

Effect of Pd Coordination and Isolation on the Catalytic Reduction of O₂ to H₂O₂ over PdAu Bimetallic Nanoparticles

Tomas Ricciardulli, Sahithi Gorthy, Jason S. Adams, Coogan Thompson, Ayman M. Karim, Matthew Neurock, and David W. Flaherty*

Cite This: *J. Am. Chem. Soc.* 2021, 143, 5445–5464

Read Online

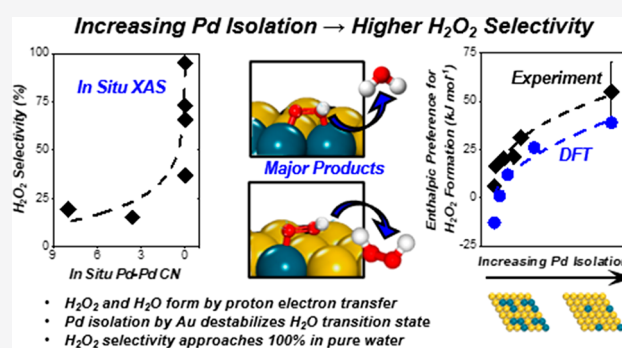
ACCESS |

Metrics & More

Article Recommendations

Supporting Information

ABSTRACT: The direct synthesis of hydrogen peroxide ($H_2 + O_2 \rightarrow H_2O_2$) may enable low-cost H_2O_2 production and reduce environmental impacts of chemical oxidations. Here, we synthesize a series of Pd_1Au_x nanoparticles (where $0 \leq x \leq 220$, ~ 10 nm) and show that, in pure water solvent, H_2O_2 selectivity increases with the Au to Pd ratio and approaches 100% for Pd_1Au_{220} . Analysis of *in situ* XAS and *ex situ* FTIR of adsorbed ^{12}CO and ^{13}CO show that materials with Au to Pd ratios of ~ 40 and greater expose only monomeric Pd species during catalysis and that the average distance between Pd monomers increases with further dilution. *Ab initio* quantum chemical simulations and experimental rate measurements indicate that both H_2O_2 and H_2O form by reduction of a common OOH^* intermediate by proton–electron transfer steps mediated by water molecules over Pd and Pd_1Au_x nanoparticles. Measured apparent activation enthalpies and calculated activation barriers for H_2O_2 and H_2O formation both increase as Pd is diluted by Au, even beyond the complete loss of Pd–Pd coordination. These effects impact H_2O formation more significantly, indicating preferential destabilization of transition states that cleave O–O bonds reflected by increasing H_2O_2 selectivities (19% on Pd; 95% on $PdAu_{220}$) but with only a 3-fold reduction in H_2O_2 formation rates. The data imply that the transition states for H_2O_2 and H_2O formation pathways differ in their coordination to the metal surface, and such differences in site requirements require that we consider second coordination shells during the design of bimetallic catalysts.



1. INTRODUCTION

Catalysts consisting of alloyed nanoparticles often provide higher rates or selectivities for desired reactions than respective pure metal catalysts.^{1–4} Particularly significant examples of industrially relevant alloyed catalysts include PdAg^{5,6} and PdPb⁷ for alkyne semihydrogenation, PtSn for alkane dehydrogenation,⁸ PdAu for vinyl acetate monomer synthesis,⁹ and PtRh for simultaneous NO_x reduction and CO and hydrocarbon oxidation.¹⁰ Differences in catalytic reactivity between monometallic and alloyed nanoparticles are frequently attributed to changes in the electronic structure caused by formation of heteronuclear metallic bonds or differences in the number and identity of reactive metal atoms present in ensembles that form active sites for catalysis. These phenomena are denoted as electronic and geometric effects, respectively.^{2,11–13} In addition, surfaces of alloy nanoparticles expose multiple metallic elements that will possess distinct binding energies for reactive species, and the resultant changes in the coverage of catalytic intermediates may influence reaction rates.¹⁴ Differences in binding energies for adsorbates between the constitutive metals in an alloy can also cause the surface structures to change in response to the chemical environment. For example, oxygen binds more strongly to Pd

than Au, and therefore, oxidative treatments tend to enrich surfaces of PdAu materials with Pd atoms in comparison to surfaces in inert environments or under vacuum.^{15–17}

Electronic effects of alloying on catalysis largely stem from changes in the d-band structure of metal surfaces due to, *inter alia*, orbital rehybridization, charge transfer, and tensile strain.^{1,2,13} The geometric effects of alloy formation in surface chemistry arise when the inclusion of a second element disrupts monometallic ensembles of contiguous metal atoms, which alters the stability of adsorbed intermediates. Multidentate organic adsorbates and reactive intermediates strongly sense these differences because charge transfer via M–O and M–C bonds between the surface and adsorbates depends upon the elemental identity of the metal.¹⁸ The adsorption of CO on Pd and PdAu surfaces provides archetypal examples: Pd predominantly binds CO at 2-fold bridge (μ^2 -CO) and 3-fold

Received: January 21, 2021

Published: April 5, 2021



hollow sites (μ^3 -CO); however, the disturbance of these ensembles drives CO to bind preferentially at atop sites (η^1 -CO) composed of Pd atoms within PdAu alloys.¹⁹

PdAu alloys can provide catalytic rates and selectivities that exceed those of monometallic Pd or Au catalysts; however, ascertaining the reasons for these differences remains a challenge. The formation of PdAu alloys modifies both the electronic and geometric structure of Pd, which has been demonstrated by investigations that involve X-ray photoelectron spectroscopy (XPS),^{20–22} X-ray absorption spectroscopy (XAS),^{20,22–37} and Fourier transform infrared spectroscopy (FTIR) of adsorbed CO.^{9,19,25,28,30,32,33,37–46} These two effects are entangled and complicate the interpretation of data obtained by these methods, because the atomic composition and arrangement of PdAu alloy surfaces affect the electronic structure. Pd and Au are miscible and form a substitutional, exothermic alloy ($-2 > \Delta H_{\text{mix}} > -9$ kJ mol⁻¹) for all compositions.^{47–49} As such, Monte Carlo simulations of PdAu surfaces predict the formation of significant numbers of isolated Pd monomers when the mole fraction of Au greatly exceeds that of Pd.^{50–52} Most results indicate that Pd atoms gain d-electrons as the Au contents in PdAu alloys increase. This conclusion agrees with clear evidence from *ex situ* XANES spectra that reveal a less intense white line at the Pd L₃ edge for Pd₁Au₁ nanoparticles compared to monometallic Pd.²² Hence, numerous spectroscopic and computational investigations indicate that alloying Pd with Au modifies the electronic structure of Pd atoms in manners that seem relevant for catalysis.

In the limit of high Au to Pd ratios (e.g., Pd₁Au₂₂₀), Pd atoms at the surface of nanoparticles exist primarily as monomers, and these materials are denoted as PdAu single-atom alloy (SAA) catalysts.⁴ SAA nanoparticles of PdAu or other combinations of elements exhibit emergent electronic and geometric properties described in recent publications.^{4,53} Valence band XPS spectra of Cu single atoms in Ag⁵⁴ and DFT calculations of electronic structure for a library of Pt, Pd, Ir, Rh, and Ni single atoms in Au, Ag, and Cu consistently show narrow *d*-bands in SAAs relative to pure metal caused by poor orbital hybridization due to a lack of homonuclear bonding materials.⁵³ These narrow *d*-bands generally give rise to greater extents of charge transfer between metal surfaces and monodentate adsorbates and more exothermic adsorption.⁵⁴ Consequently, these changes provide an opportunity to selectively destabilize multidentate surface intermediates relative to monodentate species and, thereby, significantly change rates and selectivities for catalytic reactions. Moreover, the formation of isolated active sites may reduce the translation entropy of adsorbates.⁵⁵ Recent experimental studies show that PdAu SAAs give greater rates and selectivities than monometallic Pd or Au nanoparticles for alcohol oxidation,³⁴ vinyl acetate synthesis,⁹ Ullmann coupling,⁴⁴ and selective hydrogenations of alkenes and alkynes.^{40,43}

PdAu alloys also form H₂O₂ more selectively during the direct synthesis reaction ($\text{H}_2 + \text{O}_2 \rightarrow \text{H}_2\text{O}_2$) than monometallic Pd and with much greater rates than Au.^{56,57} All known catalysts for direct synthesis form H₂O₂ by sequential oxygen reduction steps and produce water following irreversible O–O bond rupture in chemisorbed dioxygen (O₂*), hydroperoxide (OOH*), or hydrogen peroxide (H₂O₂*), such that O–O cleavage events always reduce H₂O₂ selectivities and yields.⁵⁸ Common strategies to suppress O–O bond rupture and increase H₂O₂ selectivities involve the

addition of promoters such as CO₂,^{56,57} acids,^{59,60} and halide ions such as Br^{-61,62} and Cl⁻⁵⁹. Despite their frequent use, liquid-phase acid and halide promoters present drawbacks that include catalyst deactivation by metal dissolution (leaching),⁶² the need for corrosion-resistant reactors, and challenges in purifying the product for downstream processes. An alternative strategy involves alloying the active metal (typically Pd or Pt) with another, ostensibly inert, metal to form bimetallic catalysts (e.g., PdAu,^{39,41,45,56,57,62–64} PtAg,⁶⁵ PdZn,^{60,66} PdIn,^{60,66,67} PdGa,^{60,66,67} PdSn,^{60,66} PdTe,⁶⁸ and PdSb⁶⁹). Among these bimetallic catalysts, PdAu has received the most attention.

Despite numerous investigations that report the production of H₂O₂ over PdAu nanoparticle catalysts, the molecular and kinetic basis for the increases in H₂O₂ selectivity and the quantitative relationship between rates and catalyst metal content remain controversial. Investigations consistently show that the addition of Au to Pd nanoparticles increases H₂O₂ selectivities. A fraction of the prior studies find that H₂O₂ formation rates and selectivities reach maximum values at mean atomic ratios of Pd to Au near 2;^{39,45,62,63,70–72} however, the remainder suggest that selectivities increase monotonically with the ratio of Au to Pd.^{41,45,57}

Different explanations for the method by which Au confers greater H₂O₂ selectivities to PdAu catalysts accompany each of these varied observations. First, differences in selectivities may arise from charge transfer between Au and Pd, which results in changes to the electronic structure of the exposed Pd atoms. This interpretation seems consistent with a recent study from our group that shows activation enthalpies for both H₂O₂ and H₂O formation increasing from -3 to 17 kJ mol⁻¹ and 11 to 32 kJ mol⁻¹, respectively, across a series of catalysts with metal contents varying between monometallic Pd and Pd₁Au₁₃, which correlates with an increase in H₂O₂ selectivity from 23% to 60%.⁴¹ These considerations agree also with the proposal that Au increases H₂O₂ selectivity by increasing the oxidation state of Pd based upon comparisons of kinetic data to *ex situ* XPS measurements of untreated Pd and PdAu materials,⁷³ yet contradict findings from density functional theory (DFT) and X-ray absorption near edge structure (XANES) (*vide supra*). Experimental studies typically utilize chloride precursors for Au, which leave detectable levels of Cl species that tend to oxidize metal atoms and impact reactivity.^{61,73} Second, comparisons between *in situ* XAS and rate and selectivity measurements have been taken as evidence that the greater H₂O₂ selectivity of PdAu catalysts results from the suppression of a Pd hydride phase, which has been proposed to be more active but less selective to H₂O₂ formation than metallic Pd.^{64,74} Rate measurements performed at low conversion and with *in situ* XAS⁷⁵ show that 9 nm nanoparticles of Pd atoms give much greater H₂O₂ selectivities when these exist as β -PdH_x (55% to H₂O₂) compared to when these same nanoparticles reside in a metallic state (22% to H₂O₂). Third, critical reviews of literature suggest that the dilution of Pd by Au may be responsible for the increases in selectivity,^{49,76} but little direct experimental evidence supports this hypothesis or describes if the origin of these changes are electronic or geometric effects. Fourth and finally, changes in surface composition may alter the mechanisms for H₂O₂ or H₂O formation or the identities of the most abundant reactive intermediate present at common conditions on different catalysts. To the best of our knowledge, this hypothesis has not been explicitly proposed in the literature for direct

synthesis of H_2O_2 ; however, electrochemical oxygen reduction reaction pathways, which are similar,^{75,77} can differ with catalyst and with the applied potential.^{78,79} Few studies have tested all of these hypotheses, and none have examined the possibility that reasons for the rise in H_2O_2 selectivity may change along with the Au to Pd ratio and prevailing surface motifs.

Here, we determine how Au increases selectivities for H_2O_2 formation by comparing results from steady-state measurements of H_2O_2 and H_2O formation rates on a series of highly uniform Pd_1Au_x nanoparticle ($x = 0, 3, 18, 37, 50, 220$) catalysts, detailed characterization of the structure of these nanoparticles obtained from *in situ* XAS and *ex situ* FTIR of adsorbed CO, and *ab initio* density functional theory (DFT) calculations of plausible reaction pathways on representative model surfaces. These findings show that the elementary steps and intermediates for these reactions remain constant for Pd and all Pd_1Au_x materials despite large differences in rate, selectivities, and apparent barriers for H_2O_2 and H_2O formation. These changes clearly correlate with reductions in the Pd–Pd coordination number and, at higher Au to Pd ratios, the distance between Pd monomers. Experimental measurements and DFT results agree quantitatively and demonstrate that differences between activation enthalpies for the formation of H_2O_2 and H_2O increase with the ratio of Au to Pd on nanoparticle surfaces. Those enthalpic barriers for H_2O formation increase by $\sim 60 \text{ kJ mol}^{-1}$ across this series of materials; however barriers for H_2O_2 formation change by only $\sim 20 \text{ kJ mol}^{-1}$. The differences among these barriers lead to H_2O_2 selectivities that approach 100% for the greatest Au to Pd ratios. The *d*-band structure of Pd evolves with the dilution of Pd in the $\text{PdAu}(111)$ surfaces, which prevents complete deconvolution of electronic and ensemble effects. While the *d*-band structure of $\text{Pd}(111)$ differs significantly from all $\text{PdAu}(111)$ surfaces examined, the differences among the densities of states upon Pd for the $\text{PdAu}(111)$ models are comparatively small and imply that selectivity improvements depend most directly on changes in geometric structure despite the necessary covariance of electronic and geometric structures. These comparisons provide compelling evidence that the increased selectivities for H_2O_2 reflect the differences between the active site requirements (i.e., ensemble size) for the transition states that form H_2O_2 and H_2O , which identifies the isolation of monomeric active sites as a catalyst design strategy to increase H_2O_2 selectivity.

2. MATERIALS AND METHODS

2.1. Synthesis of SiO_2 -Supported Au Nanoparticles. Silica (Sigma-Aldrich, Davisil 646, 35–60 mesh) was used as received. Au nanoparticles were deposited by a method that involved strong electrostatic adsorption of Au ethylenediamine complexes that form spontaneously following the combination of HAuCl_4 (Sigma-Aldrich, >49 wt % Au) and ethylene diamine (Sigma-Aldrich, >99%) in deionized (DI) water (>17.8 $\text{M}\Omega \text{ cm}$ resistivity). Au-SiO_2 (2.0 wt %) was prepared by dissolving HAuCl_4 (1.6 g) and ethylenediamine (5 cm^3) into DI water (100 cm^3) with the intent to exchange Cl^- ligands on Au for ethylenediamine ligands.^{19,33,80–83} A dark brown precipitate forms following the addition of ethylenediamine; however, the precipitate dissolves with stirring at ambient temperature and yields a transparent orange solution. In a separate beaker, silica (40 g) was added to a solution of deionized water (600 cm^3) and concentrated NH_4OH (100 cm^3 ; Macron, 28–30% NH_4OH). The clear solution containing gold–ethylenediamine complexes was added to the basic solution containing SiO_2 , and the resulting mixture was stirred

continuously with a plastic spatula for 10 min, followed by intermittent stirring every 10 min for 1 h to provide time for cationic Au–ethylenediamine complexes to adsorb to anionic moieties on the silica surface. The solids were filtered, washed with DI water (40 $\text{cm}^3 \text{ g}^{-1}$), and vacuum filtered to recover the damp solids. These solids were heated in a flowing (200 $\text{cm}^3 \text{ min}^{-1}$) mixture of H_2 (20 kPa; Airgas, UHP) and He (81 kPa; Airgas, UHP) to 413 at 3 K min^{-1} in a tube furnace and held at 413 K for 90 min with the intent to evaporate water and reduce the Au complexes to form uniform Au nanoparticles on silica. Samples containing different amounts of Au on silica were prepared by analogous procedures in which the ratio of HAuCl_4 to ethylenediamine and the volume of the basic solution remained constant, but the quantity of Au and silica were changed to achieve the desired Au content.

2.2. Electroless Deposition of Pd onto Supported Au Nanoparticles. Pd was selectively deposited onto the existing Au nanoparticles by electroless deposition from aqueous $\text{Pd}(\text{NO}_3)_2$ (Sigma-Aldrich, $\sim 40\%$ Pd) in an ice bath ($\sim 273 \text{ K}$).^{66,84,85} In a typical synthesis, Au-SiO_2 (5 g) was soaked for 10 min with DI water (150 cm^3) and decanted five times to remove a yellow leachate. The washed solids were transferred to a spinner flask with a suspended magnetic stir bar (used to minimize attrition of the silica particles), placed in an ice bath, and then allowed to cool for 30 min. Subsequently, an aqueous solution of $\text{Pd}(\text{NO}_3)_2$ ($\leq 0.2 \text{ mM}$ $\text{Pd}(\text{NO}_3)_2$) freshly prepared using chilled DI water (150 cm^3) was added. The mixture was blanketed with H_2 (101 kPa H_2 , 50 $\text{cm}^3 \text{ min}^{-1}$; Airgas, UHP) and constantly stirred. After continuous stirring and exposure to the blanket of H_2 gas for 3 h, the supernatant was decanted. The solids were soaked in deionized water (30 $\text{cm}^3 \text{ g}^{-1}$), decanted three times, and then dried in stagnant air at 323 K for 12 h.

These specific conditions for electroless deposition were selected to maximize the fraction of Pd that deposits selectively onto supported Au nanoparticles and not elsewhere (e.g., the gas frit or homogeneous precipitate). Note, we did not bubble H_2 into the suspension with a gas dispersion tube, because this procedure invariably deposited Pd onto the frit of the dispersion tube. In preliminary experiments, we observed that aqueous $\text{Pd}(\text{NO}_3)_2$ reduces readily in contact with H_2 to form monometallic Pd colloids in the absence of Au-SiO_2 . Nucleation theory predicts this process depends superlinearly on the concentration of Pd species,⁸⁶ while rates of electroless deposition are linear with precursor concentration and involve catalytic activation of H_2 on the pre-existing metal (i.e., Au) nanoparticles.⁸⁵ In addition, we anticipated that activation barriers to nucleate homogeneous Pd particles would be greater than for $\text{Pd}(\text{NO}_3)_2$ reduction and deposition on Au surfaces. Consequently, we chose to minimize the temperature and lower the Pd precursor concentration during the electroless deposition process to favor the deposition of Pd onto Au nanoparticles. As such, we used low Pd concentrations ($\leq 0.2 \text{ mM}$ $\text{Pd}(\text{NO}_3)_2$) and low temperatures ($\sim 273 \text{ K}$).

2.3. Synthesis of SiO_2 -Supported Pd Nanoparticles. Monometallic Pd nanoparticles were formed on silica (0.05 wt % Pd-SiO_2) by a synthesis procedure that involves strong electrostatic adsorption.⁷⁷ An aqueous solution of $\text{Pd}(\text{NO}_3)_2$ was prepared with DI water (4.7 mM, 20 cm^3). In a separate beaker, silica (20 g) was added to a mixture of DI water (350 cm^3) and concentrated NH_4OH (50 cm^3). The $\text{Pd}(\text{NO}_3)_2$ solution was added to the basic solution containing silica and stirred manually once every 30 min for 3 h. The solids were recovered, dried by vacuum filtration, and washed with DI water (500 cm^3). Subsequently, the solids were loaded into a quartz boat, heated to 673 at 3 K min^{-1} in a flowing mixture of H_2 and He (20 kPa H_2 , 81 kPa He, 100 $\text{cm}^3 \text{ min}^{-1}$) in a tube furnace, and held at 673 K for 3 h.

Nanoparticles of Pd (e.g., 1–2 nm diameters) on silica agglomerate over the course of 8–10 h during the direct synthesis reaction and form distributions of nanoparticles with larger mean diameters.⁷⁵ Therefore, we characterized monometallic Pd-SiO_2 by FTIR and TEM (*vide infra*) following steady-state catalysis at relevant conditions (55 kPa H_2 , 60 kPa O_2) for extended periods (>12 h).

2.4. Analysis of Nanoparticle Sizes by Transmission Electron Microscopy and Volumetric CO Adsorption. The

particle size distributions for each catalyst were evaluated by bright-field transmission electron microscopy using a JEOL 2010 LaB₆ operating at 200 kV. Samples were prepared by grinding the catalyst into a fine powder and dusting the powder onto copper–holey carbon TEM grids. Surface-averaged mean particle sizes were calculated using

$$\langle d \rangle_s = \frac{\sum_{i=1}^N d_i^3}{\sum_{i=1}^N d_i^2} \quad (1)$$

where d_i is the measured diameter of nanoparticle i and N is the total number of nanoparticles measured for any sample ($N > 300$). Conversely, number-averaged mean particle sizes, $\langle d \rangle_N$, are calculated as the simple average. Both values as well as the standard deviation for each catalyst are reported in Table 1. Surface-averaged calculations of

Table 1. Mean Particle Sizes and Compositions of Pd and Pd₁Au_x Catalysts

catalyst	$\langle d \rangle_s$ (nm) ^a	$\langle d \rangle_N$ (nm) ^b	standard deviation (nm)	Au content (wt %) ^c	Pd content (wt %) ^c	atomic ratio of Au to Pd ^c
Pd	3.9	3.3	1.0		0.052	0
Pd ₁ Au ₃	8.6	6.7	2.8	0.48	0.088	3
Pd ₁ Au ₁₈	9.5	7.3	2.8	2.0	0.059	18
Pd ₁ Au ₃₇	9.6	7.2	2.9	2.1	0.030	37
Pd ₁ Au ₅₀	9.4	7.5	2.7	2.1	0.022	50
Pd ₁ Au ₂₂₀	9.5	7.1	3.0	4.6	0.011	220

^aDetermined by analysis of transmission electron microscopy images using eq 1. ^bSimple average of particle sizes obtained by analysis of transmission electron microscopy images. ^cDetermined by ICP-OES (Galbraith).

mean particle size are more appropriate for catalysis applications because catalysis occurs at the nanoparticle surface. As such, surface-averaged diameters are used to estimate the numbers of surface atoms in each sample. Figure 1 presents a representative TEM image of the Pd₁Au₅₀ catalyst along with the particle size distribution for this material. The corresponding TEM images and particle size distributions for all other samples are presented in the Supporting Information (SI) (Section S3). Values of $\langle d \rangle_s$ for all Pd₁Au_x catalysts

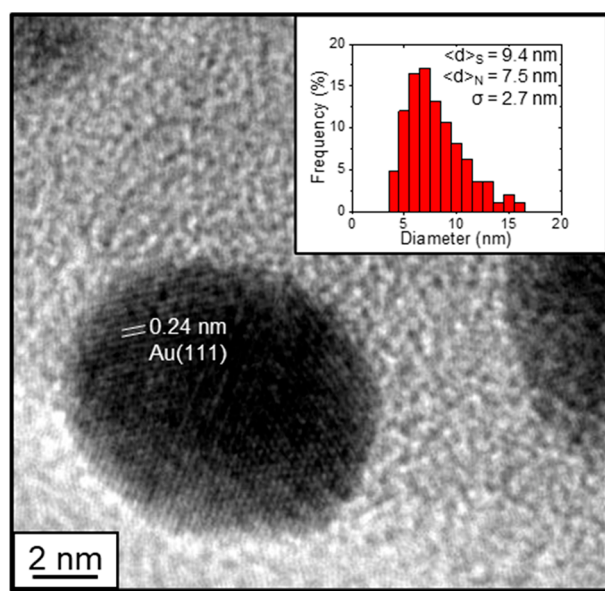


Figure 1. Representative TEM image of a Pd₁Au₅₀ nanoparticle showing lattice fringes consistent with Au(111). Inset shows the particle size distribution for this catalyst.

are similar, which indicates that differences in catalytic properties cannot be explained by differences between the size of nanoparticles.

2.5. Characterization of Catalysts by Fourier Transform Infrared Spectroscopy of Adsorbed CO. The relative numbers of Pd and Au atoms exposed on each nanoparticle, the type of atoms to which these were coordinated, and differences between the electronic states of surface Pd atoms were examined by comparisons of FTIR spectra of adsorbed ¹²CO and mixtures of adsorbed ¹²CO and ¹³CO. Samples were prepared by grinding catalysts (~60 mg) into a fine powder and pelletizing the powder into self-supporting ~20 mm diameter discs using a laboratory hydraulic press (Carver, model C). These discs were set between two stainless steel retaining rings and loaded into a custom-built transmission IR cell with CaF₂ windows, described previously.^{41,65,87–89} The cell was sealed by compressing natural graphite ferrules (Chromalytic Technology Pty. Ltd.) with another stainless steel retaining ring on the cell exterior. Gaseous H₂, ¹²CO, He, and O₂ were introduced to the cell by digital mass flow controllers (Alicat, MC Series) mounted to a gas-handling manifold connected to the cell. In comparison, ¹³CO (Sigma-Aldrich, 99% ¹³C, <5% ¹⁸O) was introduced by pulses from a custom-mixed lecture bottle (10% ¹³CO in He). A short length of steel tubing was pressurized, and each pulse of ¹³CO-He was released by briefly opening a ball valve.

Prior to adsorption of CO, all catalysts were pretreated in a combination of reductive and oxidative conditions to remove adventitious organic species and water. Pd₁Au_x catalysts were pretreated by heating to 573 at 10 K min⁻¹ in a flowing stream (30 cm³ min⁻¹) of O₂ (20 kPa) and He (81 kPa) and holding at 573 K for 1 h before cooling to 303 K in pure He. Samples were annealed in CO by heating to 383 at 10 K min⁻¹ under flowing CO (1 kPa) and He (100 kPa), holding at 383 K for 1 h, and cooling to 313 K still within 1 kPa CO. Monometallic Pd catalysts were pretreated by heating to 573 at 10 K min⁻¹ in a flowing stream (30 cm³ min⁻¹) of H₂ (20 kPa) and He (81 kPa) and holding at 573 K for 1 h. The flow of H₂ was stopped and the sample was held under pure He flow (30 cm³ min⁻¹) for 30 min before cooling to 303 K under He.

Singleton frequencies ($\nu_0(^{13}\text{C}=\text{O})$) were measured by examining a series of infrared spectra of catalysts with surfaces saturated by mixed adlayers of ¹³CO–¹²CO with a wide range of ¹³CO to ¹²CO ratios at 303 K. This was achieved by first saturating the catalyst surface in ¹³CO and incrementally dosing small amounts of ¹²CO through short pulses with a mass flow controller (0.01 cm³ min⁻¹). Surface coverages were estimated from peak intensities, and peak centers were measured directly from the spectra. The metal loading and dispersion for 0.05 wt % Pd-SiO₂ material were too small for reliable singleton frequency measurement, so a 1.0 wt % Pd-SiO₂ material was synthesized by similar methods and sintered by calcination at 673 K for 4 h in air.⁷⁷ The 0.05 and 1.0 wt % Pd-SiO₂ materials have similar surface-averaged mean diameters (~4 nm; Figure S1), although the 1.0 wt % catalyst does show a broader distribution. The two materials also show similar $\eta^1\text{-CO}^*_\text{Pd}$ peak centers (Figure S16), which suggests that the singleton frequency measurement of the 1.0 wt % material is sufficiently representative of the 0.05 wt % material, especially when compared to Pd₁Au_x.

2.6. Steady-State Formation Rate Measurements. Rates of H₂O₂ and H₂O formation were measured using a packed-bed reactor system that provides plug-flow hydrodynamics, as described elsewhere.^{41,65,66,77} Catalyst (100–1000 mg) and SiO₂ (0–900 mg, for a total of 1000 mg of catalyst and SiO₂) were loaded into a jacketed stainless steel reactor in between supporting glass wool and 4 mm diameter glass rods. Reactant gases (25% H₂ balance N₂ and 5% O₂ balance N₂ or 5% H₂ balance N₂ and UHP Air) were introduced to the system using digital mass flow controllers (Parker) and mixed with a stream of deionized and degassed H₂O (35 cm³ min⁻¹, >17.8 MΩ cm under Ar flow) fed in by an HPLC pump (SSI, M1-Class). Reaction temperatures were controlled using a refrigerated recirculating bath (Fisher Scientific, Isotemp) to flow a 50% v/v aqueous ethylene glycol solution through the reactor cooling jacket and monitored by a k-type thermocouple embedded in the reactor jacket. The reactor pressure was set by a back-pressure regulator (Equilibr,

EB1LF1-SS316) controlled by an electronic pressure reducer (Proportion Air, QBIS). The reactor effluent was split into a gas and a liquid stream using a polyvinyl chloride gas–liquid separator. The H₂ conversion was measured by analysis of the gas stream by gas chromatography (Agilent, 7890, TCD, Ar carrier and reference gas) with a packed column (Sigma-Aldrich, 3 m × 2.1 mm, molecular sieve 5A) and using N₂ as an internal standard. Samples were taken every 10 min from the liquid stream using an electronically actuated valve (Banjo Corp., LEV025PL) to deliver liquid to an electronic 10-port valve (Vici), which injected 1.0 cm³ of sample along with 1.0 cm³ of a colorimetric indicator (6 mM neocuproine, SageChem, ≥98%; 4.1 mM CuSO₄, VWR, ≥98%; 25% v/v ethanol, Decon Laboratories Inc., 100%) into test tubes held in an automated fraction collector (Biorad, 2110). The samples were then analyzed by a visible light spectrometer (Spectronic, Genesis 20, 454 nm) to determine H₂O₂ concentrations by comparison with calibration curves obtained using samples of known H₂O₂ concentration.

The effects of H₂ and O₂ pressure or temperature on product formation rates were only examined after achieving steady-state conversion for each sample, which was defined as when selectivity became invariant with time on stream (typically >3 h). In this study, selectivity is defined as the measured rate of H₂O₂ production divided by the rate of H₂ consumption.

Catalyst deactivation was corrected for by linear interpolation of time-on-stream data. Deactivation was typically small (~1% h⁻¹). Analysis of spent PdAu catalysts provides no evidence of leaching or sintering with time-on-stream. Further, *in situ* XAS indicates that the catalysts restructure on a short (<1 h) time scale; therefore, catalyst deactivation cannot be caused by replacement of surface Pd with Au. Trace organic contaminants (~1 nM) present in the solvent may be responsible for the loss of rates. Turnover rates for H₂O₂ and H₂O formation were obtained by normalizing measured product formation rates by the number of Pd atoms exposed at the surface of nanoparticles (Pd_s). Monometallic Au nanoparticles form negligible quantities of H₂O₂ under these conditions (Figure S8), likely because Au does not activate H₂ readily at these conditions.⁹⁰ Consequently, we conclude that exposed Pd atoms participate in the kinetically relevant steps for both H₂O₂ and H₂O formation. To estimate the value of Pd_s for each catalyst, we used dispersion values calculated from TEM-derived mean cluster diameters and assumed that Pd completely segregates to the surface of the nanoparticles during catalysis.

2.7. X-ray Absorption Spectroscopy Analysis of Pd Coordination. The electronic properties and local structure of Pd and PdAu catalysts were evaluated by XANES and extended X-ray absorption fine structure (EXAFS) measurements at the Pd K-edge (24350 eV) obtained using a 100-element Ge monolith fluorescence detector (Canberra) at Beamline 9-3 of the Stanford Synchrotron Radiation Light Source (SSRL). This beamline is a 16-pole, 2 T wiggler side station with vertically collimating mirror for harmonic rejection and a cylindrically bent mirror for focusing. The photon energy was selected using a liquid-nitrogen-cooled, double-crystal Si (220) $f = 90^\circ$ monochromator to scan between 24 100 and 25 100 eV. The catalyst (100 mg) was crushed to 80–120 mesh and loaded into a glassy carbon reactor (4.1 mm inner diameter, HTW Hochtemperatur-Werkstoffe GmbH) using glass wool as a mechanical support. The glassy carbon reactor was inserted into an *in situ* XAS cell⁹¹ affixed to a manifold used to deliver either gas (H₂, O₂) or H₂O (10 cm³ min⁻¹) saturated with gas (H₂, O₂).⁷⁵ The gas composition was controlled by mass flow controllers (Parker Porter, 601), which allowed gas to flow through gas dispersion frits (40–60 μm) into two pressurized saturation units (Swagelok, 304L-HDF8-2250) filled with deionized H₂O that could be operated at pressures above 6 MPa. Two HPLC pumps (SSL, MI Class) were used to mix streams of saturated H₂O from each reservoir and deliver the mixed stream containing the desired concentrations of H₂ and O₂ to the cell. The pressures of each saturator and the *in situ* cell were controlled independently by dedicated back-pressure regulators (Andon Specialties, BP3-1A11QCK11L). The XAS data for the monometallic Pd catalyst are

adapted from prior work,⁷⁵ which used a Pd-SiO₂ catalyst synthesized in a similar manner and with comparable metal loadings.

All XAS measurements were made at room temperature. Prior to XAS measurements under H₂O₂ synthesis conditions, catalysts were scanned in ambient air. Each *in situ* measurement was initiated by subsequently introducing H₂- and O₂-saturated water to the reactor via the HPLC pumps. A minimum of three spectra were collected at each set of conditions, and the spectra found to be at steady state were merged and aligned using Pd foil reference spectra collected simultaneously. Values of $\chi(k)$ were obtained by subtracting smooth atomic background from the normalized absorption coefficient using the AUTOBK code (where k is the photoelectron wavenumber). The theoretical EXAFS signals for Pd–O, Pd–Pd, and Pd–Au scattering paths were constructed using the FEFF6 code.⁹² An fcc crystal structure with a lattice constant of 3.89 Å was used to model Pd. The Pd–Au structure was constructed by replacing all the Pd atoms in the first shell of the Pd fcc structure by Au atoms. A Pd acetate trimer structure was used for Pd–O.⁹³ The theoretical EXAFS signals were fitted to the data in R -space using the Artemis program of the Demeter package using simultaneous k -weights of 1, 2, and 3. The spectra were fitted by varying the coordination number of the single scattering Pd–O and Pd–M paths (where M = Pd, or Au), the bond length disorder, the effective Pd–O/M scattering lengths, and the correction to the threshold energy, ΔE_0 . The value for the passive electron reduction factor (S_0^2) was obtained by first analyzing the spectrum for a Pd foil, and the best fit value (0.76) was fixed during the fitting. The k -range used for Fourier transform of the $\chi(k)$ was 2.6–13 Å⁻¹, and the R -range for fitting was 1.2–3.1 Å. The best parameters fit using k -weights of 1, 2, and 3 (simultaneously) in Artemis are reported; however, the results were similar to those using only a k -weight of 2. Additionally, the k -range did not have a significant effect on the best fit values of the model fit but did affect their uncertainties.

2.8. Computational Methods. First-principle density functional theory calculations were carried out to determine the energetics for the elementary adsorption, desorption, and surface reaction paths for H₂O₂ and H₂O formation over PdAu alloy surfaces within aqueous media. The calculations in the condensed phase were carried out using a density of ~1 g cm⁻³ for water in the unit cell. *Ab initio* molecular dynamics simulations were carried out for greater than 5 ps to allow the explicit water molecules to relax around the reacting molecules and generate stable reactant and product structures. These low-energy structures along the molecular dynamics trajectory were used to establish representative model structures to conduct subsequent static DFT calculations to determine the reaction energies and activation barriers.

All of the simulations were carried out using plane wave DFT as implemented in the Vienna *ab initio* simulation program (VASP).^{94–96} Plane waves were constructed with an energy cutoff of 396 eV along with projector augmented wave potentials (PAW) to model interactions between core and valence electrons.^{97,98} The generalized gradient approximation (GGA) along with the Perdew–Burke–Ernzerhof functional were used to determine the exchange and correlation gradient corrections, and the D3 method of Grimme was used to characterize van der Waals interactions and capture the dispersive interactions in the local environment.^{99–101}

Wave functions were optimized in a self-consistent manner and converged to within 10⁻⁶ eV using a gamma centered 3 × 3 × 1 k -point mesh grid. The atomic positions were optimized and converged to a point where the maximum force on each atom was less than 0.1 eV Å⁻¹. A two-step approach was used to isolate the transition states and calculate the activation barriers.

The first step used the climbing nudged elastic band method to optimize the energies for a series of structures along the reaction path using a force tolerance of 0.1 eV Å⁻¹. The highest energy structures were subsequently used as input to the dimer method to isolate the transition-state structures and were converged until the forces dropped below 0.08 eV Å⁻¹.^{102–104}

2.9. Creation of Model Surfaces. To discern the catalytic consequences of isolating Pd atoms in Au, reaction energies and

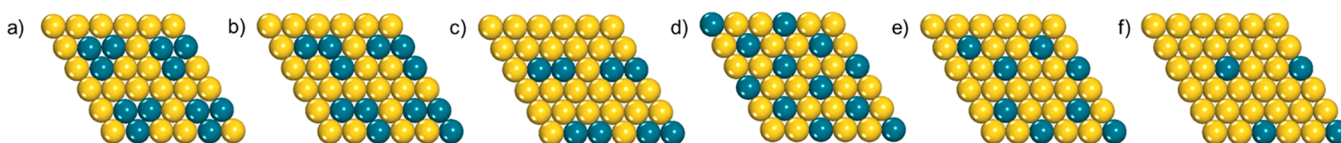


Figure 2. Pd atom distributions on Au(111) slabs that include (a) equilateral close-packed Pd trimers, (b) open Pd trimers, (c) Pd dimers, (d) paired Pd monomers with six Pd next-nearest neighbors (NNN = 6), (e) paired Pd monomers with three Pd next-nearest neighbors (NNN = 3), and (f) isolated Pd monomers with exclusively Au atoms at nearest and next-nearest neighbor positions (NNN = 0).

activation barriers for the formation of H_2O_2 and H_2O (by decomposition of OOH^*) from H_2 and O_2 on six different surfaces comprised of Au and Pd atoms were calculated. Figure 2 shows the model surfaces examined, which include predominantly Au slabs that contains Pd trimers (Figure 2a,b) or dimers (Figure 2c) and three different forms of Pd monomers (Figure 2d–f). Comparisons between reaction energies and barriers calculated on these surfaces reflect the effects of differences in the nearest-neighbor Pd–Pd coordination number (NN, $1 \leq \text{NN} < 2$) and in the next-nearest-neighbor Pd–Pd coordination number (NNN, $0 \leq \text{NNN} \leq 6$) on O_2 reduction. Among these models, a single Pd atom with NN and NNN values equal to zero (Figure 2f) was selected to represent the behavior of the most dilute PdAu surfaces.

While previous studies suggest that high coverages of oxygen on Pd surfaces significantly modify energy barriers to promote H_2O_2 formation,^{75,105,106} *in situ* characterization of PdAu surfaces (Section 3.2) suggests that such high coverages do not form under the studied conditions. Additionally, the differing numbers of Pd atoms in the model slabs (Figure 2) complicate consistent interpretation of coverage effects for all coverages other than zero, as such reaction barriers and energetics are calculated considering an otherwise empty surface.

All calculations were carried out using periodic slabs consisting of a 3×3 unit cell with four layers of the Au(111) surface by replacing surface Au atoms with Pd atoms according to the above description and optimizing the metal slab before adding the solvent layers. The bottom two layers of the slab were held fixed at bulk positions of the Au lattice, while the top two layers were allowed to relax fully. A vacuum region of ~ 15 Å between the topmost and bottom metal layers was used in all the condensed-phase calculations to allow the solvent molecules to relax.

The densities of states (DOS) for the different surfaces examined herein were calculated in two steps. In the first step, structural optimizations and single-point energy calculations for the slab were carried out using a k -point grid of $6 \times 6 \times 1$ with an energy convergence of 10^{-6} eV and until the force on each atom was below 0.05 eV. In the second step, the DOS was calculated using a higher k -point grid of $12 \times 12 \times 1$. The d -band center reported was calculated as the first moment of the d -band. The data for a Pd(111) surface are adapted from reference 75, which employed identical methods to calculate DOS.

3. RESULTS AND DISCUSSION

3.1. Effect of Au to Pd Ratio within Nanoparticles on Rates and Selectivities for H_2O_2 Formation. To understand the effects of dispersing Pd atoms on Au nanoparticles, we measured primary H_2O_2 formation rates and selectivities across the series of uniform Pd and Pd_1Au_x nanoparticle catalysts ($0 \leq x \leq 220$) supported on silica. Figure 3 shows that both turnover rates for H_2O_2 formation and the H_2O_2 selectivities depend on the atomic ratio of Au to Pd across this series of catalysts (55 kPa H_2 , 60 kPa O_2 , 286 K). H_2O_2 turnover rates decrease by 3-fold (0.37 to 0.12 mol H_2O_2 mol Pd_s^{-1} s $^{-1}$) across this range of materials as the ratios of Au to Pd increase. Measured turnover rates generally decrease but possess noticeable scatter with the addition of Au, which arises from significant uncertainty in estimates for the number of

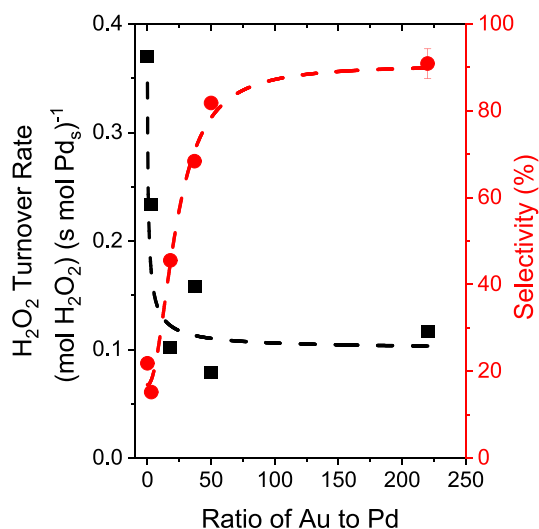


Figure 3. Steady-state H_2O_2 turnover rates (black ■) and primary H_2O_2 selectivities (red ●) for Pd and Pd_1Au_x catalysts with a range of Au to Pd atomic ratios ($0 \leq x \leq 220$) at standard conditions (55 kPa H_2 , 60 kPa O_2 , 286 K).

active sites on these materials (Supporting Information Section S5). To circumvent this complication, we focus primarily on kinetic parameters that do not depend upon estimates for the number of sites including H_2O_2 selectivities, apparent activation enthalpies, and changes in rates as functions of reactant concentrations. These decreases in H_2O_2 turnover rates coincide with a nearly monotonic increase in H_2O_2 selectivities ranging from $19 \pm 1\%$ for Pd to $95 \pm 3\%$ for $\text{Pd}_1\text{Au}_{220}$. Nanoparticles of Pd_1Au_3 deviate from this trend and provide H_2O_2 selectivities ($15 \pm 1\%$) slightly lower than monometallic Pd ($19 \pm 1\%$); these Pd_1Au_3 nanoparticles predominantly expose Pd atoms at their surfaces with Au-rich subsurfaces and, therefore, possess significant surface Pd–Pd coordination (*vide infra*) with electronic modifications caused by the Au subsurface. Larger atomic ratios of Au to Pd ($x > 18$) provide significant increases in H_2O_2 selectivities, and this nonmonotonic trend suggests that Au influences the reactivity of Pd in multiple ways. These H_2O_2 selectivities are lower than previous reports of catalysts with similar elemental compositions,^{39,41,45,56,57,107} which likely originates from differences in the experimental conditions (i.e., temperature, solvent composition, promoters, reactor type). For example, many studies implement alcohol solvents and one or more forms of promoters (e.g., mineral acids^{59,60} and halides^{59,61,62}) that frequently increase H_2O_2 selectivities but complicate fundamental investigations. The results in Figure 3 suggest that the increases in primary H_2O_2 selectivities and decreases in turnover rates may reflect differences in the structural motifs of Pd active sites, the electronic characteristics of these active sites, or the mechanism of the reactions that produce H_2O_2

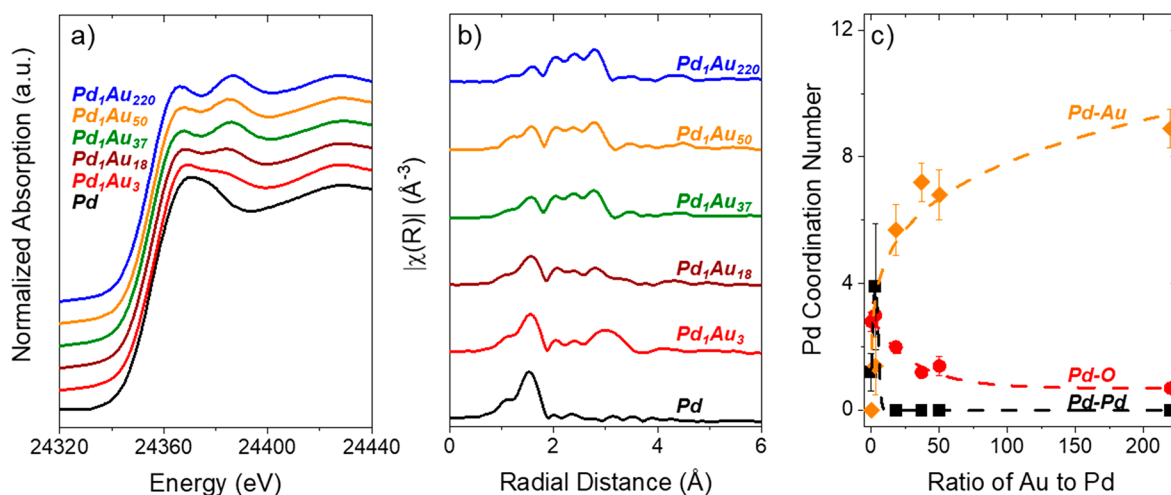


Figure 4. (a) XANES spectra and (b) EXAFS magnitude of the Fourier-transformed k^2 -weighted $\chi(k)$ data ($k = 2.7\text{--}13 \text{ \AA}^{-1}$) for Pd (black), Pd_1Au_3 (red), $\text{Pd}_1\text{Au}_{18}$ (brown), $\text{Pd}_1\text{Au}_{37}$ (green), $\text{Pd}_1\text{Au}_{50}$ (gold), and $\text{Pd}_1\text{Au}_{220}$ (blue) and (c) EXAFS best fit Pd–Pd (black ■), Pd–Au (gold ◆), and Pd–O (red ●) coordination as a function of the atomic ratio of Au to Pd measured *ex situ* (ambient air, 298 K).

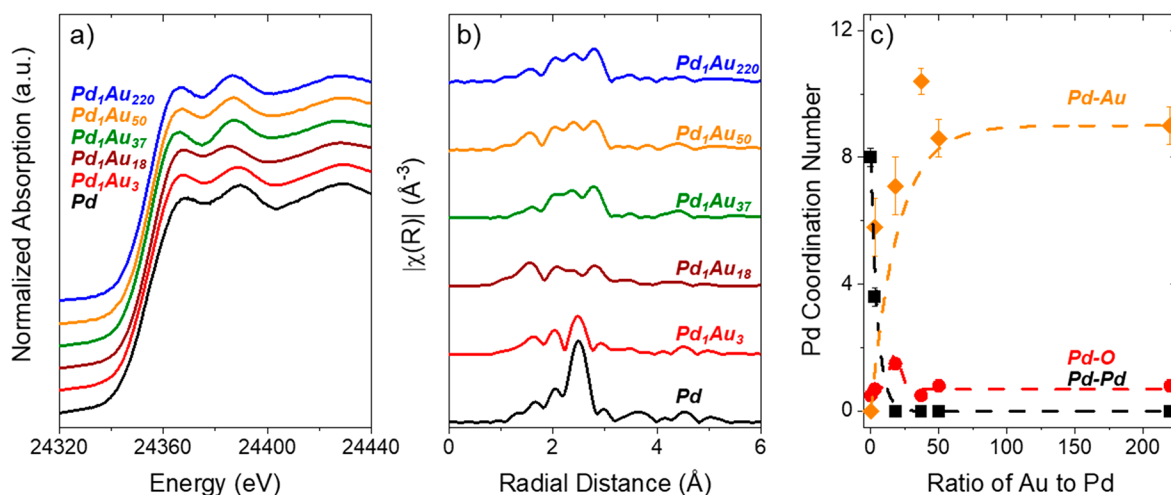


Figure 5. (a) XANES spectra and (b) EXAFS magnitude of the Fourier-transformed k^2 -weighted $\chi(k)$ data ($k = 2.7\text{--}13 \text{ \AA}^{-1}$) for Pd (black), Pd_1Au_3 (red), $\text{Pd}_1\text{Au}_{18}$ (brown), $\text{Pd}_1\text{Au}_{37}$ (green), $\text{Pd}_1\text{Au}_{50}$ (gold), and $\text{Pd}_1\text{Au}_{220}$ (blue) and (c) EXAFS best fit Pd–Pd (black ■), Pd–Au (gold ◆), and Pd–O (red ●) coordination numbers as a function of the atomic ratio of Au to Pd measured *in situ* (55 kPa H_2 , 60 kPa O_2 , 298 K).

and H_2O among these six catalysts as a result of changes in the Au to Pd atomic ratio. We examine these possibilities using X-ray absorption spectroscopy, detailed measurements of catalytic rate as functions of reactant concentrations and temperature, and *ab initio* quantum calculations on representative model surfaces in the presence of the solvent.

3.2. Characterization of Pd Coordination by X-ray Absorption Spectroscopy. Figure 4 shows the *ex situ* Pd K-edge XANES spectra, FT-EXAFS in R-space, and EXAFS best-fit coordination numbers for each catalyst obtained from catalysts previously subjected to oxidative thermal treatments (1 h, 5 K min^{-1} , 573 K, $100 \text{ cm}^3 \text{ min}^{-1}$ air) and held within ambient conditions (air, $\sim 295 \text{ K}$). The normalized XANES spectra (Figure 4a) show a slightly lower white-line intensity for materials with high Au to Pd (0.98 for $\text{Pd}_1\text{Au}_{220}$) ratios in comparison to Pd (1.07) and Pd_1Au_3 (1.03). In addition, the amplitude of the oscillations above the K-edge indicates that Pd atoms in the Pd_1Au_x materials possess lower total coordination numbers than in monometallic Pd nanoparticles or Pd foil, which implies that Pd exists predominantly at the

surfaces of the nanoparticles. Analysis of all *ex situ* spectra shows a large amount of Pd–O coordination that results from the oxidative pretreatment and exposure to air while collecting spectra. The average Pd–O coordination number decreases as the Au to Pd ratio increases (e.g., $N_{\text{Pd-O}} = 3$ on Pd_1Au_3 and $N_{\text{Pd-O}} = 0.5$ on $\text{Pd}_1\text{Au}_{220}$), and intensities of XANES white lines decrease simultaneously (Figure 4a). These changes suggest that coordination of Pd to Au reduces the propensity of Pd to oxidize. Taken together, the low Pd–Pd and Pd–Au coordination numbers and significant Pd–O coordination indicate that the Pd_1Au_3 and $\text{Pd}_1\text{Au}_{18}$ catalysts contain segregated domains of oxidized Pd on the exterior of Au nanoparticles.

These results demonstrate that the extent of alloying depends strongly on composition under oxidizing conditions.

The direct synthesis of H_2O_2 requires a combination of H_2 and O_2 co-reactants, and consequently, the structure and chemical states of Pd and Pd_1Au_x nanoparticles may change in response. Figure 5 shows results from *in situ* XANES and EXAFS that reveal that the structure of these Pd and Pd_1Au_x

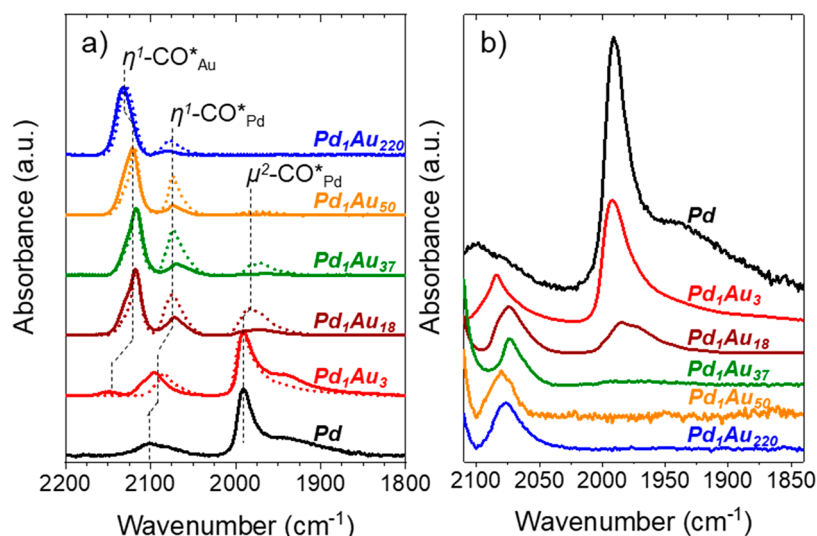


Figure 6. Infrared spectra of CO*-saturated surfaces of Pd (black), Pd₁Au₃ (red), Pd₁Au₁₈ (brown), Pd₁Au₃₇ (green), Pd₁Au₅₀ (gold), and Pd₁Au₂₂₀ (blue) catalysts (0.02 kPa CO, 303 K). (a) Spectra following initial CO exposure (solid lines) and after annealing in CO (dashed lines; 1 h, 1 kPa CO, 373 K). All spectra normalized by the maximum intensity. (b) Infrared spectra after annealing in CO (1 kPa CO, 373 K, 1 h) normalized by the intensity of the η¹-CO*_{Pd} feature.

catalysts at relevant conditions (55 kPa H₂, 60 kPa O₂, 298 K) differs significantly from those observed *ex situ*. The *in situ* XANES results (Figure 5a) show a decrease in the white-line intensity of the monometallic Pd and Pd₁Au₃ catalysts only, and all have similar white-line intensity. Additionally, the magnitude of the EXAFS spectra (Figure 5b) and the Pd coordination numbers (Figure 5c) differ considerably from observations made *ex situ*. Differences between *ex situ* and *in situ* XAS of the Pd and Pd₁Au_x nanoparticles demonstrate that the reaction conditions decrease values of $N_{\text{Pd-O}}$ and reduce Pd to a predominately metallic state, which agrees with prior *in situ* XAS performed on Pd and PdAu nanoparticles during direct synthesis.^{74,75} Values of $N_{\text{Pd-Au}}$ measured *in situ* exceed those obtained *ex situ* for each Pd₁Au_x material, which demonstrates that these reaction conditions cause Pd to alloy with Au once Pd reduces, suggesting that Pd could be segregated on the surface of Au as PdO_x domains. Across the series of Pd₁Au_x materials, $N_{\text{Pd-Au}}$ initially increases with the atomic ratio of Au to Pd from a value of 6 for Pd₁Au₃ to values near 9 for Pd₁Au₃₇ and above. Coordination between Pd atoms cannot be detected (i.e., $N_{\text{Pd-Pd}} \sim 0$) for any bimetallic material aside from Pd₁Au₃. Consequently, the total coordination number for Pd falls between 7 and 10 for all Pd₁Au_x materials, which is significantly lower than the coordination number of Pd in the bulk of a face centered cubic structure ($N_{\text{Pd-Pd}} = 12$). These results indicate that the majority of Pd atoms reside at the surfaces of Pd₁Au_x nanoparticles, which agrees with prior experimental and theoretical studies that examined the structure of PdAu alloys in the presence of O₂.¹⁵⁻¹⁷ Figure 5c shows that most PdAu catalysts possess $N_{\text{Pd-O}}$ values near or slightly less than 1, which suggests that oxygen-derived intermediates may saturate these Pd sites during catalysis (*vide infra*). The data for Pd₁Au₁₈ deviate slightly from the trends observed in the other Pd₁Au_x catalysts, which suggests differences in structure between this material and the other Pd₁Au_x materials. The Pd₁Au₁₈ catalyst shows no measurable Pd-Pd coordination and greater $N_{\text{Pd-O}}$ than the other Pd₁Au_x catalysts *in situ*; however, $N_{\text{Pd-Pd}}$ becomes 0.7 after reductive treatments (Table S5). This comparison

suggests that the segregated domains of oxidized Pd on Au persist in this catalyst under reaction conditions.

Taken together, the Pd coordination numbers obtained *in situ* (Figure 5c) strongly suggest that surfaces of Pd₁Au₃₇, Pd₁Au₅₀, and Pd₁Au₂₂₀ catalysts primarily consist of Au with very low mole fractions of Pd. Within these surfaces, Pd primarily exists as monomers and possibly a few Pd nearest neighbors that could not be detected by EXAFS due to their low concentration compared with Pd-Au. As such, these nanoparticles form single-atom alloys during catalysis. The differences in turnover rates for the formation of H₂O₂ and H₂O and the selectivities toward H₂O₂ for this series of Pd and Pd₁Au_x catalysts (Figure 3) likely reflect the changes in coordination number for Pd observed *in situ* (Figure 5). However, rates and selectivities differ between Pd₁Au₃₇, Pd₁Au₅₀, and Pd₁Au₂₂₀ despite the strong similarities in the structure of these materials determined by EXAFS. However, a comparison of the XANES spectra in Figure S18 shows measurable differences at 24375 eV, suggesting that the Pd environment is slightly modified as the Au to Pd ratio increases. EXAFS analysis of the next-nearest neighbors was dominated by Pd-Au scattering and resulted in large uncertainties for the number of Pd atoms in the second coordination shell. Consequently, we hypothesize that next-nearest-neighbor interactions (i.e., the second coordination shell of Pd atoms in Au), which challenge EXAFS analysis, appear to impact catalysis. To test this hypothesis, we developed an experimental approach to examine structure and proximity of exposed Pd atoms beyond the first coordination shell.

3.3. Analysis of Pd and Pd₁Au_x Nanoparticle Structure by Infrared Spectra of Adsorbed CO. Figure 6 shows steady-state infrared spectra of CO adsorbed to the surfaces of Pd and Pd₁Au_x catalysts (0.02 kPa CO, 303 K) following *in situ* oxidative (20 kPa O₂, 573 K, 1 h) or reductive (1 kPa CO, 373 K, 1 h for PdAu_x and 20 kPa H₂, 673 K, 1 h for Pd) treatments designed to change the segregation and dispersion of Pd atoms at the surface. These treatments consistently yield infrared spectra that show three distinct

binding configurations for CO*. Absorption features between 2130 and 2110 cm^{-1} correspond to CO linearly bound to Au atoms ($\eta^1\text{-CO}^*_{\text{Au}}$), peaks between 2100 and 2070 cm^{-1} arise from CO linearly bound atop Pd atoms ($\eta^1\text{-CO}^*_{\text{Pd}}$), and peaks below 2000 cm^{-1} reflect CO adsorbed at bridge ($\mu^2\text{-CO}^*_{\text{Pd}}$) and 3-fold hollow ($\mu^3\text{-CO}^*_{\text{Pd}}$) sites formed by ensembles of Pd atoms.^{19,33,40,42,43,45,108}

After oxidative treatments, the FTIR spectra of adsorbed CO show clear differences between the catalysts. Across the series of materials, the peak areas of $\eta^1\text{-CO}^*_{\text{Au}}$ relative to $\eta^1\text{-CO}^*_{\text{Pd}}$ and $\mu^2\text{-CO}^*_{\text{Pd}}$ increase with the Au to Pd ratio, reflecting increasing enrichment of surfaces with Au. The $\eta^1\text{-CO}^*_{\text{Pd}}$ peak red-shifts by $\sim 27 \text{ cm}^{-1}$ between Pd to Pd₁Au₃₇, which agrees with red-shifts attributed to a mixture of ligand and ensemble effects in prior studies.^{42,43,109} We analyze differences in $\eta^1\text{-CO}^*_{\text{Pd}}$ features in greater detail later (Section 3.4). The Pd₁Au₃₇, Pd₁Au₅₀, and Pd₁Au₂₂₀ catalysts show little or no $\mu^2\text{-CO}^*_{\text{Pd}}$, which suggests that these materials predominantly expose atomically disperse Pd after oxidative treatments and agrees with the interpretation of Pd coordination numbers derived from EXAFS (Section 3.2). In contrast, the spectrum for Pd₁Au₃ shows a combination of a $\mu^2\text{-CO}^*_{\text{Pd}}$ and a $\eta^1\text{-CO}^*_{\text{Pd}}$ feature, the combined area of which exceeds that for $\eta^1\text{-CO}^*_{\text{Au}}$ by a factor of 45, which indicates that Pd₁Au₃ nanoparticles predominantly expose Pd and few Au atoms and may resemble core–shell structures.

Reductive treatments in CO (1 kPa CO, 373 K, 1 h) induce significant structural changes that appear in the vibrational features of CO* subsequently adsorbed (Figure 5; 0.02 kPa, 303 K). The reductive treatment increases the peak area of $\eta^1\text{-CO}^*_{\text{Pd}}$ and $\mu^2\text{-CO}^*_{\text{Pd}}$ and decreases the intensity of $\eta^1\text{-CO}^*_{\text{Au}}$ for all Pd₁Au_x nanoparticles relative to spectra obtained after oxidative treatments. These changes demonstrate that CO exposure at moderate temperature enriches Pd₁Au_x nanoparticle surfaces in Pd. On Pd₁Au₃, the $\eta^1\text{-CO}^*_{\text{Pd}}$ feature red-shifts by 12 cm^{-1} and peaks for $\eta^1\text{-CO}^*_{\text{Au}}$ and $\mu^3\text{-CO}^*_{\text{Pd}}$ (shoulder at 1940 cm^{-1}) disappear as a consequence of restructuring. This red-shift in $\eta^1\text{-CO}^*_{\text{Pd}}$ exceeds the shift caused by dipole coupling alone (*vide infra*, Figure 7), which signifies a change in the electronic structure of the exposed Pd atoms in this catalyst. The other Pd₁Au_x catalysts present shifts in the $\eta^1\text{-CO}^*_{\text{Pd}}$ feature of 2 cm^{-1} or less, representing small differences in dipole–dipole coupling or the electronic structure of Pd. The thermal treatment also causes the Pd₁Au₃₇ and Pd₁Au₅₀ catalysts to show detectable amounts of $\mu^2\text{-CO}^*_{\text{Pd}}$, which is consistent with the change in EXAFS for Pd₁Au₁₈ under a CO atmosphere (Table S5) and demonstrates that Pd oligomers form at the surfaces of these materials. This results from the increased coverage of Pd atoms and the greater stability of $\mu^2\text{-CO}^*_{\text{Pd}}$ and $\mu^3\text{-CO}^*_{\text{Pd}}$ configurations that involve Pd dimers and oligomers in comparison to $\eta^1\text{-CO}^*_{\text{Pd}}$ on bimetallic Pd₁Au_x surfaces.^{110–112}

The relative populations of monomeric and oligomeric Pd atoms on surfaces of Pd₁Au_x nanoparticles and their sensitivity to the chemical environment can be examined by quantifying the ratio (ρ) of areas for features corresponding to $\eta^1\text{-CO}^*_{\text{Pd}}$ and $\mu^2\text{-CO}^*_{\text{Pd}}$ prior to annealing in CO (after only oxidative or reductive treatments, Section 2.5) and following treatments in CO (1 kPa CO, 373 K, 1 h). Table 2 shows that values of ρ for Pd and Pd₁Au_x materials increase monotonically with the Au to Pd ratio regardless of the pretreatment conditions.

Values of ρ decrease following treatment in CO for Pd₁Au_x materials with Au to Pd ratios of 18 and greater, because CO*

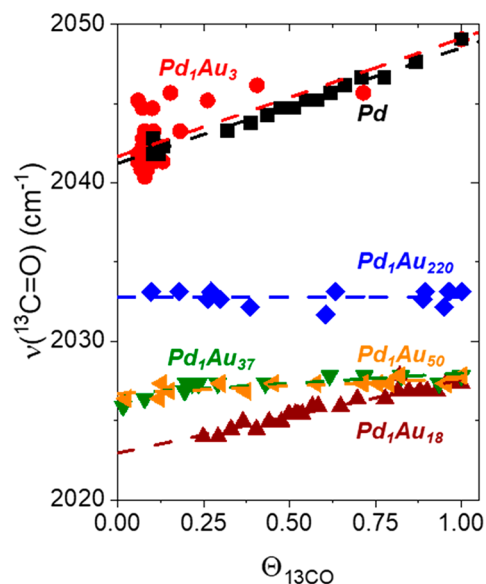


Figure 7. Vibrational frequency for the $\nu(\text{C}=\text{O})$ mode of $\eta^1\text{-}^{13}\text{CO}^*_{\text{Pd}}$ as a function of the fractional coverage of $^{13}\text{CO}^*$ on monometallic Pd (■), Pd₁Au₃ (red ●), Pd₁Au₁₈ (brown ▲), Pd₁Au₃₇ (green ▼), Pd₁Au₅₀ (gold ◀), and Pd₁Au₂₂₀ (blue ◆) at 303 K. Dashed lines indicate linear fits to data.

Table 2. Ratio (ρ) of $\eta^1\text{-CO}^*_{\text{Pd}}$ to $\mu^2\text{-CO}^*_{\text{Pd}}$ Peak Area for Pd and Pd₁Au_x Catalysts before and after Annealing in CO

catalyst	ρ	
	before annealing in CO ^{a,b}	after annealing in CO ^{a,c}
Pd	0.1	n. a.
Pd ₁ Au ₃	0.3	0.3
Pd ₁ Au ₁₈	1.8	1.0
Pd ₁ Au ₃₇	7.9	5.7
Pd ₁ Au ₅₀	>50 ^d	14
Pd ₁ Au ₂₂₀	>50 ^d	>50 ^d

^aMeasured in 0.02 kPa CO at 303 K. ^bPretreated in 20 kPa O₂, 573 K, 1 h for Pd₁Au_x or in 20 kPa H₂, 573 K, 1 h for Pd. ^cPretreated in 1 kPa CO, 373 K, 1 h. ^dThese spectra show no detectable $\mu^2\text{-CO}^*_{\text{Pd}}$; reported values are instead lower bounds estimated from the signal-to-noise ratios of each spectra.

stabilizes greater fractions of Pd at the surfaces of these nanoparticles. Among these CO-treated nanoparticles, ρ consistently increases with the Au to Pd ratio and becomes greater than 50 for Pd₁Au₂₂₀, which suggests that Pd exists predominantly as monomers after reduction in CO for this material only. These trends agree with expectations from Monte Carlo simulations that account for differences in the stability of Pd–Pd and Pd–Au bond strengths in predictions for the distribution of Pd atoms among monomeric and oligomeric surface species as functions of the fractional coverage of Pd in equilibrated PdAu(111) surfaces.^{50,51} Hence the decrease in ρ and increase in $\eta^1\text{-CO}^*_{\text{Au}}$ area, relative to both $\eta^1\text{-CO}^*_{\text{Pd}}$ and $\mu^2\text{-CO}^*_{\text{Pd}}$, show that the Pd surface coverage decreases systematically with increases in the Au to Pd ratio. *In situ* XAS, however, indicates that nearly all Pd atoms within the Pd₁Au₃₇, Pd₁Au₅₀, and Pd₁Au₂₂₀ catalysts reside on the nanoparticle surface as monomers (i.e., $N_{\text{Pd-Pd}} \sim 0$) (Figure 5). Consequently, these comparisons between XAS and FTIR of CO* species suggest that the separation between Pd monomers increases with the Au to Pd ratio.

3.4. Probing Changes in Geometric and Electronic Structure of Exposed Pd Atoms via Infrared Spectra of Mixed ^{12}CO and ^{13}CO Adlayers.

Values of the vibrational frequencies measured for the $\nu(\text{C}=\text{O})$ mode of CO^* species on transition metal surfaces depend upon the extent of electron donation and back-donation between CO and the metal surface but also dipole–dipole coupling between adsorbed CO molecules (i.e., the vibrational Stark effect).^{12,113} These effects can be deconvoluted by independently changing the significance of dipole–dipole coupling between CO^* species by the adsorption of mixtures of ^{13}CO and ^{12}CO .^{11,12} As one example, the individual contributions of electron exchange with the surface and the magnitude of dipole–dipole coupling can be assessed by measuring changes in the frequency of $\nu(^{13}\text{C}=\text{O})$ for $\eta^1\text{-CO}^*_{\text{Pd}}$ as a function of fractional coverage of ^{13}CO ($\theta_{^{13}\text{CO}}$) in a saturated monolayer of ^{12}CO and ^{13}CO (i.e., $\theta_{^{12}\text{CO}} + \theta_{^{13}\text{CO}} = 1$).^{12,114} This analysis uses the relationship

$$\nu(^{13}\text{C}=\text{O}) = \nu_0 + \theta_{^{13}\text{CO}}\Delta\nu \quad (2)$$

where the intercept ν_0 represents the singleton frequency (i.e., $\nu(^{13}\text{C}=\text{O})$ in the absence of dipole–dipole coupling) and reports on the electronic structure of the binding site, and $\Delta\nu$ quantifies the shift caused by dipole–dipole coupling, which depends on the inverse-cube of distance between comparable CO^* species.^{113,114}

Figure 7 shows that values of $\nu(^{13}\text{C}=\text{O})$ depend linearly upon $\theta_{^{13}\text{CO}}$ for the Pd and Pd_1Au_x catalysts after oxidative treatments (20 kPa O_2 , 573 K, 1 h), which agrees with the form of eq 2. In each experiment, the nanoparticle surfaces were initially saturated with $^{13}\text{CO}^*$, which was subsequently displaced using small pulses of ^{12}CO (Section 2.5.). Our analysis considers $\eta^1\text{-CO}^*$ on Pd, because this feature appears on all catalysts and can be readily deconvoluted from the other peaks present. The values of ν_0 do not depend monotonically on the ratio of Au to Pd (Table 3); however, nanoparticles with Au to Pd ratios of 18 and greater exhibit lower values than pure Pd.

Table 3. Dipole Coupling Shifts ($\Delta\nu$) and Singleton Frequencies (ν_0) of $\eta^1\text{-}^{13}\text{CO}^*_{\text{Pd}}$ for Pd and Pd_1Au_x Catalysts

catalyst	$\Delta\nu$ (cm^{-1})	ν_0 (cm^{-1})
Pd	7.3 ± 0.2	2041 ± 1
Pd_1Au_3	7.5 ± 1.3	2042 ± 1
$\text{Pd}_1\text{Au}_{18}$	4.6 ± 0.3	2023 ± 1
$\text{Pd}_1\text{Au}_{37}$	1.3 ± 0.4	2027 ± 1
$\text{Pd}_1\text{Au}_{50}$	0.9 ± 0.2	2027 ± 1
$\text{Pd}_1\text{Au}_{220}$	0.0 ± 0.4	2033 ± 1

These comparisons show that the interactions between Pd and Au clearly induce an electronic modification to the Pd present at the surface and resemble findings from similar measurements made on PdAu/Pd(111) single-crystal surface alloys at 290 K.¹¹⁵ Singleton frequency shifts from 2041 cm^{-1} for monometallic Pd to 2023 cm^{-1} for $\text{Pd}_1\text{Au}_{18}$, but further increases of the catalyst Au content cause an increase of the singleton frequency to 2033 cm^{-1} for $\text{Pd}_1\text{Au}_{220}$. These observations seem consistent with nonmonotonic changes in the Pd *d*-band structure with surface Au content observed by core-level XPS of PdAu films annealed at various temperatures²¹ and Pd K-edge white-line intensities of carbon-supported PdAu nanoparticles with Au to Pd ratios between 0 and 5.¹¹⁶ Comparing the Pd_1Au_x catalysts with Au to Pd ratios

of 18 to 50, the values of ν_0 are too similar to adequately differentiate the catalysts. The $\text{Pd}_1\text{Au}_{220}$ catalyst shows a slightly higher ν_0 (2033 cm^{-1}), which may imply a slightly different electronic structure of the Pd atoms in this sample, although the direct effect of this difference on catalysis cannot be ascertained from this measurement alone.

The values of $\Delta\nu$ (Table 3, 0.0–7.3 cm^{-1}) are much smaller than those obtained from similar experiments on Pt and PtAg catalysts and low-index Pt single crystals^{65,114,117} but similar to those measured on PdAu/Pd(111) single-crystal surface alloys and Pt(335) single crystals.^{115,117} These differences reflect the fact that dipole–dipole coupling requires similar vibrational frequencies,^{11,12} which indicates that $\eta^1\text{-CO}^*_{\text{Pd}}$ will only couple with other $\eta^1\text{-CO}^*_{\text{Pd}}$ but not other forms of CO^* . Monometallic Pd nanoparticles predominantly present $\eta^1\text{-CO}^*_{\text{Pd}}$ at defect, edge, and corner sites; however, Pt surfaces form $\eta^1\text{-CO}^*_{\text{Pt}}$ at the majority of terrace sites.¹¹³ These terrace sites possess greater surface coordination than edge sites and thus show more significant effects of dipole–dipole coupling.

While the values of ν_0 show a complex dependence on the composition of Pd_1Au_x nanoparticles, the extent of dipole–dipole coupling (quantified by $\Delta\nu$) decreases monotonically with an increase in the ratio of Au to Pd (Table 3) from 7.3 ± 0.2 cm^{-1} on monometallic Pd to 0.0 ± 0.4 cm^{-1} on $\text{Pd}_1\text{Au}_{220}$. This trend holds also for $\text{Pd}_1\text{Au}_{37}$, $\text{Pd}_1\text{Au}_{50}$, and $\text{Pd}_1\text{Au}_{220}$ catalysts, which yield indistinguishable Pd coordination numbers (i.e., $N_{\text{Pd-Pd}}$, $N_{\text{Pd-Au}}$) from *in situ* XAS. Considering the inverse-cube dependence of dipole coupling shift values on average distances between sites,^{113,114} this decrease provides strong evidence for an increase in the average distance between $\eta^1\text{-CO}^*_{\text{Pd}}$ sites and, therefore, changes in the second coordination shell of Pd as the Au to Pd ratio increases.

3.5. Computational Evidence that H_2O_2 Forms by Heterolytic Pathways on PdAu. In previous sections, we characterized the means through which the formation of Pd_1Au_x alloys affect the properties of Pd. These modifications may influence the mechanisms responsible for catalytic formation of H_2O_2 and H_2O . Therefore, we combine computational and experimental methods to determine the molecular processes that form H_2O_2 and H_2O on Pd_1Au_x catalysts.

Lunsford and co-workers showed that negligible quantities of $\text{H}^{18}\text{O}^{16}\text{OH}$ form during reactions of $^{18}\text{O}_2$ and $^{16}\text{O}_2$ with H_2 on Pd, which indicates that H_2O_2 proceeds through reduction of an OOH^* intermediate and that O–O bonds cleave irreversibly.¹¹⁸ Within water, these reduction processes have been proposed to occur either through homolytic Langmuirian surface reactions that involve direct addition of H atoms or by solvent-mediated processes involving proton–electron transfer through H_3O^+ species. We demonstrated that OOH^* and H_2O_2^* formation by direct addition of the surface-bound hydrogen atoms defined herein as H (note, # and * indicate that the OH_x intermediates and H species bind to separate sites as discussed in Section 3.6) to dioxygen intermediates on Pd(111) present energy barriers 14 and 19 kJ mol^{-1} higher than the analogous proton–electron transfer (PET) steps.⁷⁵ PdAu(111) surfaces, however, may or may not exhibit the same preference for PET pathways to reduce oxygen.

Figure 8 shows the intrinsic barriers (ΔE^\ddagger), reaction energies (ΔE_{rxn}) and optimized reactant, transition and product structures for OOH^* and H_2O_2^* formation by homolytic (Figure 8a and c) and heterolytic (Figure 8b and d) processes on isolated Pd monomers on the Au(111)

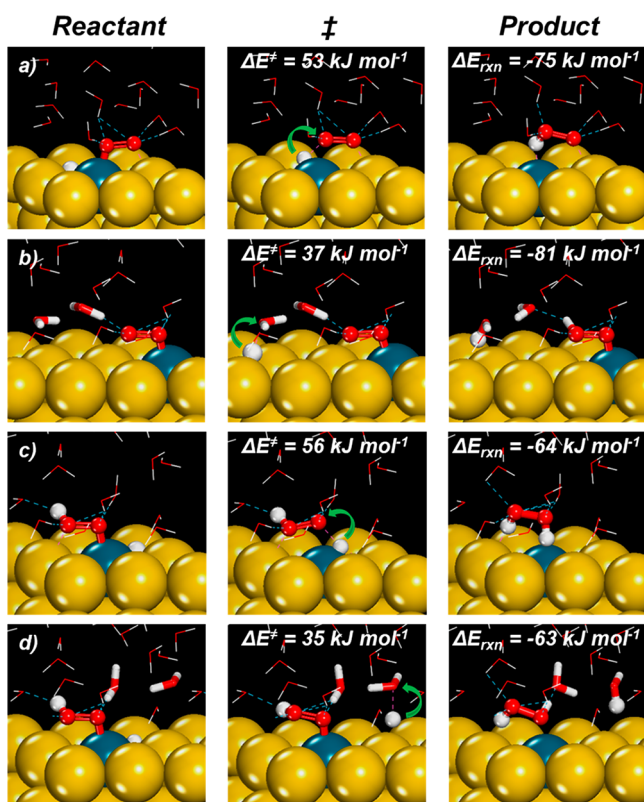


Figure 8. Reactant, transition, and product state structures and activation energies and overall reaction energies for (a, b) OOH* and (c, d) H₂O₂* formation by (a, c) direct surface H[#] transfer and (b, d) H₂O-mediated proton electron transfer on an isolated Pd monomer surface (Figure 2f).

surface. Proton–electron transfer pathways that involve multiple explicit water molecules (i.e., a Grotthuss-type mechanism) such as those shown in Figure 8b and d report lower intrinsic activation energies (ΔE^\ddagger) for OOH* and H₂O₂* formation than those carried out by local H[#] addition such as those shown in Figure 8a and c, by 16 and 21 kJ mol⁻¹, respectively. These differences in ΔE^\ddagger agree with similar differences calculated on Pd(111)⁷⁵ and indicate that product formation on both Pd₁Au_x (presenting either monomeric or oligomeric Pd atoms) and Pd catalysts occurs through similar heterolytic, solvent-mediated mechanisms.

Bader charge analysis of the surface species and the metal surface at multiple positions along the reaction coordinate provides further evidence that oxygen reduction involves heterolytic processes involving charged intermediates. Figure 9 shows the charge distribution between the different species for the OOH* and H₂O₂* formation reactions through proton–electron transfer (solid lines) and homolytic surface reactions (dotted lines). In the PET mechanism, a surface H[#] atom oxidizes heterolytically and forms a proton that transfers to liquid water and an electron that is transferred to the metal and donated or shared with the bound O₂* or OOH* intermediate. Subsequently, the hydronium intermediate that forms during proton addition transfers one of its protons to O₂* or OOH*. The charge on this protic hydrogen remains constant at 0.7 e⁻ during the transfer reaction. Near the completion of each reaction, the charge on O₂* or OOH* decreases slightly due to proton transfer from H₃O⁺. Both heterolytic and homolytic pathways display identical charge distribution for the reactive

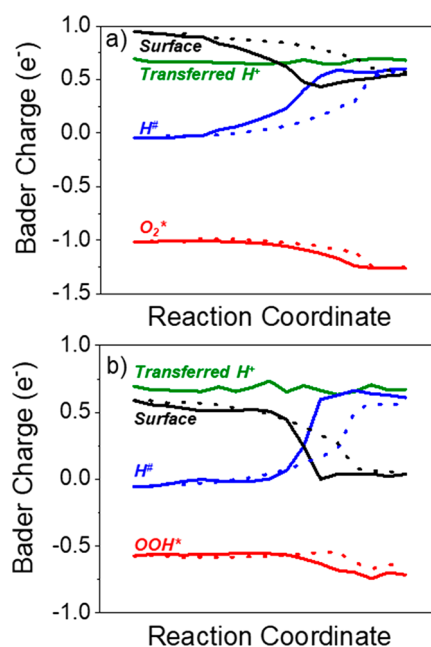


Figure 9. Bader charge profiles of O₂* or OOH* (red), H[#] (blue), the H atom being transferred (green), and the metal surface (black) during (a) O₂* reduction to OOH* and (b) OOH* reduction to H₂O₂* via a heterolytic PET-type mechanism (solid lines) and via a homolytic hydrogen transfer type mechanism (dashed lines). Calculations performed on an open Pd trimer surface (Figure 2b) in aqueous media.

species at the reactant and product states; however, the nature of the H atoms in the transition state differs. The positive charge carried by the protic H atoms of water leads to barriers for PET that are consistently lower than those for direct H[#] atom transfer. In direct H[#] atom transfer, the H[#] atom transferred develops a positive charge gradually and only becomes protic after its complete addition to O₂* or OOH*.

3.6. Effects of H₂ and O₂ Pressures on Steady-State H₂O₂ and H₂O Formation Rates and Interpretation. Figures 10 and 11 show turnover rates for H₂O₂ and H₂O formation as functions of H₂ (Figures 10a and 11a; 20–400 kPa H₂, 60 kPa O₂) and O₂ pressure (Figure 10b and 11b, 20–400 kPa O₂, 55 kPa H₂) for monometallic Pd, Pd₁Au₃, and Pd₁Au₂₂₀ catalysts in deionized water. Rates of H₂O₂ formation increase linearly with H₂ pressure ($r_{\text{H}_2\text{O}_2} \sim [\text{H}_2]^1$) at lower values (<100 kPa H₂) and become constant ($r_{\text{H}_2\text{O}_2} \sim [\text{H}_2]^0$) at higher values (>150 kPa H₂) (Figure 10a). Turnover rates for H₂O formation (Figure 11a) also increase linearly with H₂ pressure at low values of [H₂] (<100 kPa) but do not change significantly at higher values (>150 kPa). Formation rates for H₂O₂ and H₂O do not depend on O₂ pressure ($r \sim [\text{O}_2]^0$) across the wide range of conditions examined (Figures 10b and 11b), which suggests oxygen-derived species saturate active sites that form both products. Further, on both monometallic Pd⁷⁷ and alloyed Pd₁Au₂₂₀ (Figure S25), protic solvents are required to form H₂O₂, because turnover rates are immeasurably small in aprotic solvents, such as dimethyl sulfoxide and acetonitrile. The requirement for protic solvents and the dependence of rates on reactant pressures agree with our previous reports on Pd and Pd-based bimetallic catalysts.^{41,65,66,75,77} These experimental findings agree with the conclusions from comparisons between *ab initio* calculations for heterolytic and homolytic pathways (Figure 8) and provide

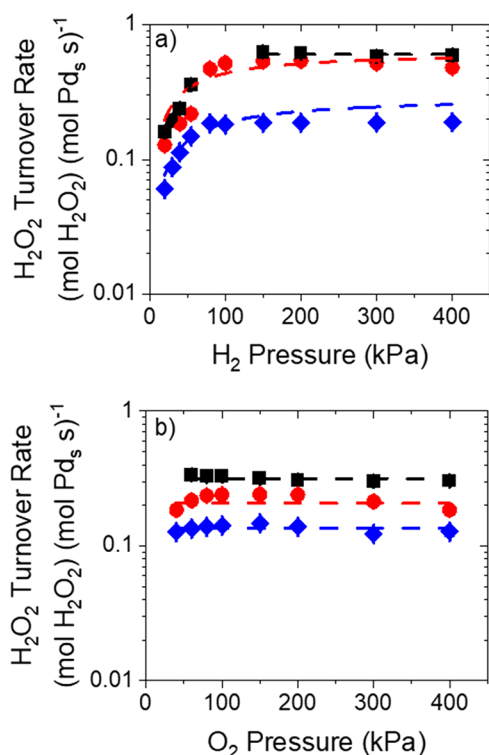


Figure 10. Turnover rates for H₂O₂ formation for monometallic Pd (black ■, 276 K), Pd₁Au₃ (red ●, 276 K), and Pd₁Au₂₂₀ (blue ◆, 291 K) as a function of (a) H₂ pressure (60 kPa O₂) and (b) O₂ pressure (55 kPa H₂). Dashed lines indicate fits to eqs 7 and 8 for H₂O₂ and H₂O formation, respectively. Rates for Pd₁Au₂₂₀ were measured at a higher temperature because H₂O formation rates are immeasurably small for this catalyst at 276 K (Figure S10).

further evidence that H₂O₂ and H₂O form through similar proton–electron transfer pathways and reactive intermediates on Pd and also Pd₁Au_x catalysts.

Scheme 1 shows a system of elementary steps that form H₂O₂ and H₂O by kinetically relevant proton–electron transfer steps and which reproduces the dependence of rates on H₂ and O₂ pressures. This scheme considers two types of sites (* and #) that account for the preference of oxygenated intermediates and H[#]-atoms to bind at distinct positions on close-packed surfaces (* sites bind oxygenates, and # sites bind H[#] atoms). Similar two-site kinetic models accurately describe measured power laws in ethylene hydrogenation, where C₂H_y^{*} and H[#] species do not competitively adsorb on Pt catalysts, as indicated by kinetic regimes in which rates are uninhibited by exceptionally high H₂ pressures.¹¹⁹ These two-site kinetic models may be further justified by differences in the preferred binding sites of H atoms and oxygenates on Pd surfaces calculated by DFT^{58,75,106} and are rationalized in terms of the differing steric and electronic properties of the two “classes” of adsorbates. Alternatively, the ethylene hydrogenation rates (and also the results in Figures 10 and 11) may be explained by realizing that intrinsic rate constants depend on the coverages of adsorbates.¹²⁰ Here, we elect to use a two-site model that captures the known site preferences of the relevant intermediates and which provides the minimum level of complexity needed to describe measured H₂O₂ and H₂O turnover rates.

The formation of H₂O₂ and H₂O involves dissociative adsorption of H₂ (step 1) onto unoccupied #sites to form

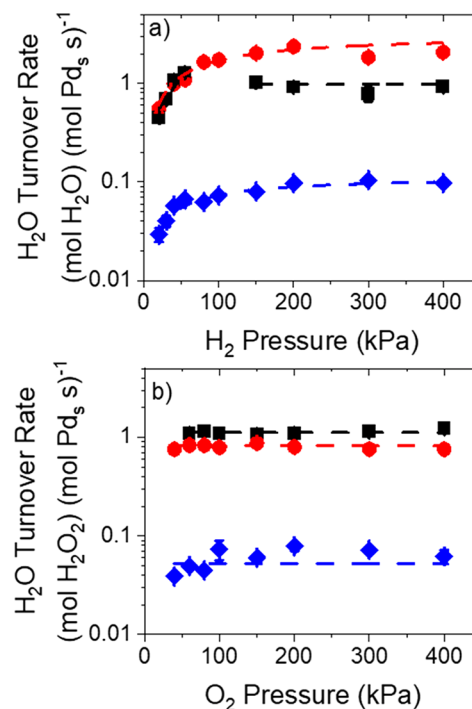
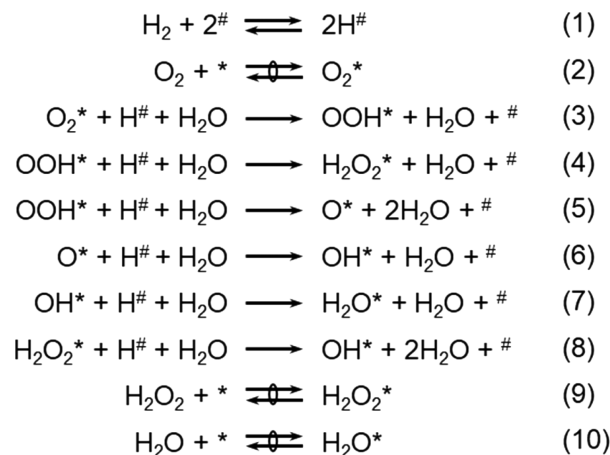


Figure 11. Turnover rates for H₂O formation for monometallic Pd (■, 276 K), Pd₁Au₃ (red ●, 276 K), and Pd₁Au₂₂₀ (blue ◆, 291 K) as a function of (a) H₂ pressure (60 kPa O₂) and (b) O₂ pressure (55 kPa H₂). Dashed lines indicate fits to eqs 7 and 8 for H₂O₂ and H₂O formation, respectively. Rates for Pd₁Au₂₂₀ were measured at a higher temperature because H₂O formation rates are immeasurably small for this catalyst at 276 K (Figure S10).

Scheme 1. Proposed System of Elementary Steps Describing H₂O₂ and H₂O Formation on Pd and Pd₁Au_x Nanoparticles^a



^aThe symbol \rightarrow denotes an irreversible reaction, whereas \rightleftharpoons signifies a reversible reaction and \rightleftharpoons with an ellipse corresponds to a quasi-equilibrated reaction.

chemisorbed H[#] atoms. Simultaneously, O₂ adsorbs in a quasi-equilibrated manner to form O₂^{*} (step 2), which then undergoes irreversible proton–electron transfer involving H[#] atoms and liquid-phase H₂O to form OOH^{*} (step 3). Subsequently, OOH^{*} reduces further by a second proton–electron transfer event to form either H₂O₂^{*} when the O–O bond persists (step 4) or H₂O and O^{*} when the O–O bond

cleaves (step 5). Notably, O–O bonds rupture irreversibly, and hence the O* species must form H₂O.^{41,65,66,75,77} This process occurs by sequential proton–electron transfer events that form OH* (step 6) and ultimately H₂O* (step 7). Adsorbed H₂O₂* and H₂O* undergo quasi-equilibrated desorption to yield detectable products (steps 9 and 10, respectively).

Scheme 1 proposes that both H₂O₂ and H₂O form by irreversible reactions that involve H₂O-assisted reduction of oxygenates by H[#] atoms. These reactions occur in series following a common kinetically relevant step: the reduction of O₂* to OOH* (step 3). Consequently, the rate of O₂ consumption follows the relationships

$$-r_{\text{O}_2} = r_3 = \frac{r_{\text{H}_2\text{O}}}{2} + r_{\text{H}_2\text{O}_2} \quad (3)$$

where the individual product formation rates are

$$r_{\text{H}_2\text{O}_2} = \frac{k_4}{k_4 + k_5} r_3 \quad (4)$$

and

$$r_{\text{H}_2\text{O}} = 2 \frac{k_5}{k_4 + k_5} r_3 \quad (5)$$

Within this system, the rate of step 3 is given by

$$r_3 = k_3 [\text{O}_2^*] [\text{H}^\#] [\text{H}_2\text{O}] \quad (6)$$

where k_3 is the intrinsic rate constant for step 3, $[\text{H}_2\text{O}]$ is the concentration of H₂O (55 M), and $[\text{O}_2^*]$ and $[\text{H}^\#]$ correspond to the numbers of O₂* and H[#] surface intermediates. Equation 6 can be restated as a function of reactant pressures and intrinsic rate constants by applying the pseudo-steady-state hypothesis to the coverages of reactive intermediates (OOH*, O*, OH*, H[#]) and invoking a site balance for each type of active site. The complete forms of the resulting rate expressions and the associated derivations are shown in Supporting Information Section S8.

These complex equations simplify in the limit of high $[\text{O}_2]$ to $[\text{H}_2]$ ratios where #sites remain unoccupied and H₂ activates irreversibly ($r_1 \gg r_{-1}$) to yield the forms

$$\frac{r_{\text{H}_2\text{O}_2}}{[\text{L}]} = \frac{k_{\text{app,H}_2\text{O}_2} [\text{H}_2]}{1 + K_{\text{app}} [\text{H}_2]} \quad (7)$$

and

$$\frac{r_{\text{H}_2\text{O}}}{[\text{L}]} = \frac{k_{\text{app,H}_2\text{O}} [\text{H}_2]}{1 + K_{\text{app}} [\text{H}_2]} \quad (8)$$

where the apparent rate constant for H₂O₂ formation appears as

$$k_{\text{app,H}_2\text{O}_2} = \frac{k_1 k_4}{k_4 + 2k_5} \quad (9)$$

and the apparent rate constant for H₂O formation is

$$k_{\text{app,H}_2\text{O}} = \frac{2k_1 k_5}{k_4 + 2k_5} \quad (10)$$

The form of the apparent adsorption constant contains numerous rate constants:

$$K_{\text{app}} = \frac{k_1 \left(\frac{k_4 + k_5}{k_4 + 2k_5} \right) \left(1 + \frac{k_3}{k_4 + k_5} + \frac{k_3 k_3}{(k_4 + k_5)} \left(\frac{1}{k_6} + \frac{1}{k_7} \right) \right)}{k_3 [\text{H}_2\text{O}]} \quad (11)$$

where k_i corresponds to the intrinsic rate constant for reaction i in Scheme 1 and $[\text{L}]$ represents the number of active sites. Equations 7 and 8 predict that rates will increase linearly with H₂ pressure at low H₂ pressure, become independent of H₂ pressure at higher H₂ pressures, and maintain constant values with changes in O₂ pressure. These predictions adequately describe H₂O₂ and H₂O formation rates on Pd₁Au_x catalysts (Figures 10 and 11) and observations from previous reports,⁸ where at low H₂ pressures rates monotonically increase before approaching constant values at higher H₂ pressures. The differences between the apparent dependence of rates on $[\text{H}_2]$ in the two limits reflect a change in most abundant reactive intermediate (MARI) from unoccupied #sites to H[#]. Rates do not depend on $[\text{O}_2]$, because *sites remain nearly saturated by a mixture of O₂*, O*, OH*, and OOH* at all conditions examined here. The rate expressions in eqs 7 and 8 capture all measurements obtained on Pd₁Au_x materials but do not fully agree with rates measured on monometallic Pd nanoparticles. These discrepancies relate to a discontinuity in measured turnover rates on Pd most clearly observed in Figure 11a (H₂O formation rates drop sharply between 55 and 150 kPa H₂). This discontinuity in rates and selectivities on Pd correlates with a phase transition between metallic Pd and β -PdH_x that appears clearly in the analysis of *in situ* EXAFS.^{74,75} Unsurprisingly, comparatively simple rate expressions (e.g., eqs 7 and 8) cannot account for such phase transitions and the associated differences in rate constants. *In situ* EXAFS shows that Pd atoms remain metallic in all Pd and Pd₁Au_x catalysts under conditions where rates increase linearly with H₂ pressure (Figure 5; 55 kPa H₂, 60 kPa O₂). Consequently, the suppression of β -PdH_x formation cannot explain high H₂O₂ selectivities on Pd₁Au_x catalysts shown in Figure 3 (e.g., 19 ± 1% for Pd, 95 ± 3% for Pd₁Au₂₂₀).

3.7. Effects of Pd Dilution by Au on Energy Barriers for H₂O₂ and H₂O Formation. The dilution of Pd by Au does not change the mechanism by which H₂O₂ and H₂O form, and comparisons of H₂O₂ selectivities over metallic Pd and Pd₁Au_x exclude prior hypotheses regarding the formation of the β -PdH_x phase. Therefore, the dependence of rates and selectivities on the Au to Pd ratio likely stems from differences in the intrinsic activation barriers for H₂O₂ and H₂O formation.

Table 4 shows calculated energy barriers and reaction energies for OOH* formation from O₂* and H[#] (i.e., O₂* + H[#] + H₂O → OOH* + # + H₂O) on each Pd₁Au_x surface. As the number of Pd atoms involved in the 3-fold hollow adsorption ensemble for H[#] decreases from three to one, the reaction becomes more exothermic by 47 kJ mol⁻¹. Diluting Pd further destabilizes H[#], leading to an additional 11 kJ mol⁻¹ released by the reaction. However, dilution of Pd by Au leads to an increase in the intrinsic barrier from 24 to 37 kJ mol⁻¹ across the series of surfaces. The increased barriers reflect greater difficulty for the heterolytic oxidation of H[#] into a proton–electron pair as the reaction ensemble includes more Au atoms, which increases the number of electrons in the metal, lowers the electron affinity (i.e., the work function) of the metal, and inhibits electron transfer.¹²¹

Table 4. Reaction Energies and Intrinsic Activation Barriers for H₂O-Mediated Hydrogenation of O₂* to Form OOH* (O₂* + H[#] + H₂O → H₂O + [#] + OOH*)

surface	ΔE_{rxn} (kJ mol ⁻¹)	ΔE^\ddagger (kJ mol ⁻¹)
closed Pd trimer ^a	-23	24
open Pd trimer ^b	-22	27
Pd dimer	-55	30
paired Pd monomer (NNN = 6) ^c	-70	34
paired Pd monomer (NNN = 3) ^d	-75	39
isolated Pd monomer (NNN = 0) ^e	-81	37

^aClosed equilateral triangular ensemble of Pd atoms in Au (Figure 2a). ^bOpen triangular ensemble of three contiguous Pd atoms in Au (Figure 2b). ^cSurface with six Pd next-nearest neighbors (Figure 2d). ^dSurface with three Pd next-nearest neighbors (Figure 2e). ^ePd atoms with no Pd nearest or next-nearest neighbors (Figure 2f).

Figure 12a shows calculated energy diagrams for OOH* reduction to form H₂O₂ through solvent-mediated proton–electron transfer (i.e., OOH* + H[#] + H₂O → H₂O₂* + [#] + H₂O) on each PdAu_x(111) surface. Similar to OOH* formation, increasing isolation of Pd causes ΔE_{rxn} to decrease (become more negative) and ΔE^\ddagger to increase for the H₂O₂ formation reaction as seen in Figure 12a. The reaction becomes more exothermic due to destabilizing H[#] by including Au in the adsorption ensemble. Intrinsic barriers increase from 19 to 35 kJ mol⁻¹, reflecting differences in electron affinities and work functions between Pd and Au. In the transition state (Figure 8d) for this reaction, on all PdAu(111) surfaces, OOH* is adsorbed in a η^1 configuration on Pd and only weakly senses neighboring atoms because it is not formally bound to them.

In Scheme 1, primary H₂O₂ selectivity is determined by competing reactions that reduce OOH* to H₂O₂ or H₂O. Figure 12b shows the energetics of H₂O formation by cleaving OOH* through solvent-mediated proton–electron transfer (i.e., OOH* + H[#] + H₂O → O* + [#] + 2H₂O) on each surface. The O* species reduces further to H₂O through subsequent proton–electron transfer events (Scheme 1). Unlike OOH* and H₂O₂ formation, ΔE_{rxn} increases as Pd is isolated from -199 kJ mol⁻¹ on the closed Pd trimer surface to -158 kJ mol⁻¹ on the Pd isolated monomer surface. These changes result from a decreased binding energy for O* as the surface ensemble required to bind the product contains more Au

atoms. The intrinsic barrier for this reaction increases from 6 to 74 kJ mol⁻¹ as Pd is isolated by Au, a significantly larger change than we observed for OOH* and H₂O₂ formation. Figure 13 shows the reactant, product, and transition-state

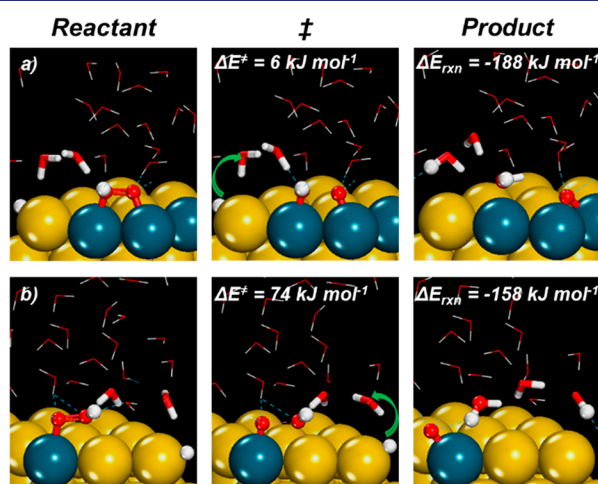


Figure 13. Reactant, transition, and product states for H₂O formation by solvent-mediated proton–electron transfer (i.e., OOH* + H[#] + H₂O → 2H₂O + O* + [#]) on (a) open Pd trimers and (b) isolated Pd monomers on PdAu(111) surfaces.

structures for H₂O formation on both the open Pd trimer and isolated monomer surfaces. In this reaction, the O–OH bond ruptures after electron transfer to form the O–OH⁽⁻⁾ transition state, which then accepts a proton from H₃O⁺ to make H₂O. This transition state involves multiple surface atoms required to adsorb O* and OH^{(-)*} after O–O bond scission and is, as such, more sensitive to the surface metal coordination because both O* and OH^{(-)*} bind much more weakly on more Au-rich ensembles. Thus, increasing the isolation of Pd allows us to selectively destabilize this H₂O transition state, which involves multiple surface atoms, relative to the H₂O₂ formation transition state, which only binds to one surface atom, ultimately increasing the H₂O₂ selectivity.

Figure 14 shows the apparent activation enthalpies for H₂O₂ and H₂O ($\Delta H_{\text{H}_2\text{O}_2}^\ddagger$ and $\Delta H_{\text{H}_2\text{O}}^\ddagger$, respectively) formation (55 kPa H₂, 60 kPa O₂, 276–306 K). These measurements were obtained at conditions where rates of H₂O₂ and H₂O

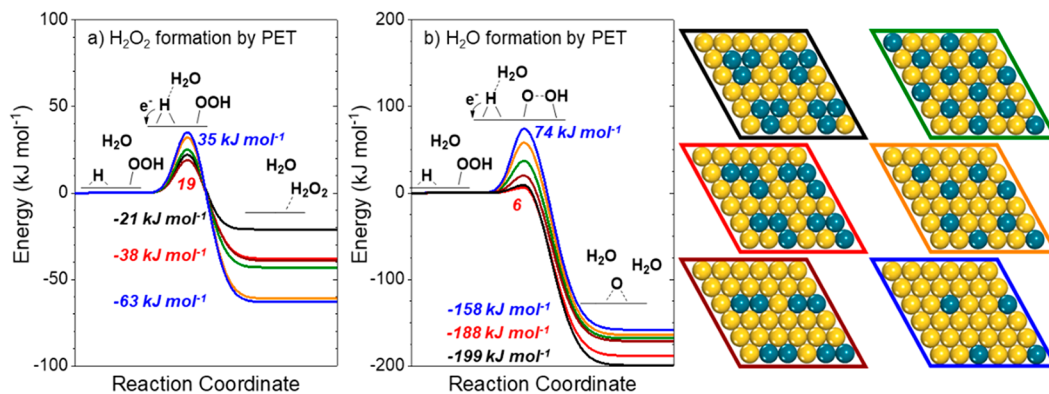


Figure 12. DFT-calculated reaction coordinate diagrams for (a) H₂O₂ and (b) H₂O formation over closed triangular Pd trimers (black), open Pd trimers (red), dimers (brown), paired monomers with six Pd next-nearest neighbors (NNN = 6, green), paired Pd monomers with three Pd next-nearest neighbors (NNN = 3, gold), and isolated Pd monomers with exclusively Au atoms at nearest and next-nearest-neighbor positions (NNN = 0, blue) on Au surfaces. Insets show structures for reactant, transition, and product states.

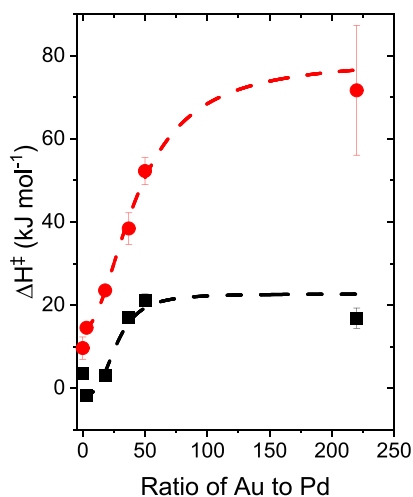


Figure 14. Change in apparent activation enthalpies for H₂O₂ (black ■) and H₂O (red ●) formation with Pd and PdAu catalyst metal content (55 kPa H₂, 60 kPa O₂, 276–306 K).

formation increase linearly with H₂ pressure, which signifies that coverages of H[#] species are insignificant. Then, the rate expressions for H₂O₂ and H₂O formation (eqs 7 and 8) collapse to simpler forms:

$$\frac{r_{\text{H}_2\text{O}_2}}{[\text{L}]} = \frac{k_1 k_4 [\text{H}_2]}{k_4 + 2k_5} \quad (12)$$

and

$$\frac{r_{\text{H}_2\text{O}}}{[\text{L}]} = \frac{2k_1 k_5 [\text{H}_2]}{k_4 + 2k_5} \quad (13)$$

These expressions show that rates for H₂O₂ and H₂O formation depend only on [H₂] and rates constants for steps 1, 4, and 5, because these elementary steps determine the coverage of the reactive OOH* intermediate and the rates at which this species reacts to form each product. By extension, ΔH[‡]_{H₂O₂} and ΔH[‡]_{H₂O} are functions of the intrinsic activation enthalpies for H₂ activation, OOH* reduction to H₂O₂, and OOH* reduction to H₂O. However, the complex forms of eqs 12 and 13 prevent precise molecular interpretations of experimental values for ΔH[‡]_{H₂O₂} and ΔH[‡]_{H₂O}.

Despite these complications, the rate expressions, and therefore the definitions of apparent activation enthalpy, remain constant across all catalysts examined in this study, so ΔH[‡]_{H₂O₂} and ΔH[‡]_{H₂O} may be compared to one another in a physically meaningful way. Values of ΔH[‡]_{H₂O} increase as a strong function of Au to Pd ratio from Pd (10 ± 3 kJ mol⁻¹) to Pd₁Au₂₂₀ (72 ± 16 kJ mol⁻¹), yet ΔH[‡]_{H₂O₂} values increase by only ~15 kJ mol⁻¹. Notably, ΔH[‡]_{H₂O} values increase monotonically while ΔH[‡]_{H₂O₂} initially increase with the Au to Pd ratio but then approach constant values for Au to Pd ratios of 37 to 220. These comparisons demonstrate that the high H₂O₂ selectivities observed on Pd₁Au_x materials (Figure 3) reflect the preferential destabilization of transition states that cleave the O–O bond within OOH* intermediates, which agrees with the results from DFT calculations on representative surfaces (Figure 12). The monometallic Pd catalyst exhibits low ΔH[‡] values (<15 kJ mol⁻¹) for both reactions, consistent with previous reports from our group.^{65,66,75,77} The Pd₁Au₃ catalyst exhibits similar selectivities and ΔH[‡] values to the monometallic Pd catalyst for both reactions. Character-

ization results from FTIR of adsorbed CO and *in situ* EXAFS show significant amounts of Pd–Pd surface coordination in this catalyst, indicating the increases in ΔH[‡] values, and therefore selectivity, result from an absence of Pd–Pd surface coordination.

While differences in ΔH[‡]_{H₂O₂} and ΔH[‡]_{H₂O} values between catalysts cannot be precisely attributed to the intrinsic barriers for specific steps in Scheme 1, the difference between ΔH[‡]_{H₂O₂} and ΔH[‡]_{H₂O} can be (Supporting Information Section S8.3), as the rate ratio of H₂O₂ to H₂O formation takes the form

$$\frac{r_{\text{H}_2\text{O}_2}}{r_{\text{H}_2\text{O}}} = \frac{k_4}{2k_5} \quad (14)$$

which implies that the difference (ΔΔH[‡]) between the experimentally measured apparent barriers ΔH[‡]_{H₂O₂} and ΔH[‡]_{H₂O} is equal to the difference between intrinsic barriers ΔH[‡]₄ and ΔH[‡]₅. ΔΔH[‡] represents the difference between the stability of the transition states for steps 4 and 5 (Scheme 1), because both H₂O₂ and H₂O form by reactions among the same intermediates (H[#], OOH*, and H₂O). Importantly, experimentally measured ΔΔH[‡] values may be directly compared to differences in intrinsic barriers calculated by DFT and do not require the assumptions made in Section 3.4 to simplify eqs 7 and 8.

Figure 15 shows the differences between the intrinsic barriers for steps 4 and 5 obtained by both theory and experiment for multiple PdAu(111) surfaces and Pd₁Au_x catalysts. In both cases, the difference in apparent barriers increases with the Au content, indicating an increasing enthalpic preference for the H₂O₂ transition state over the

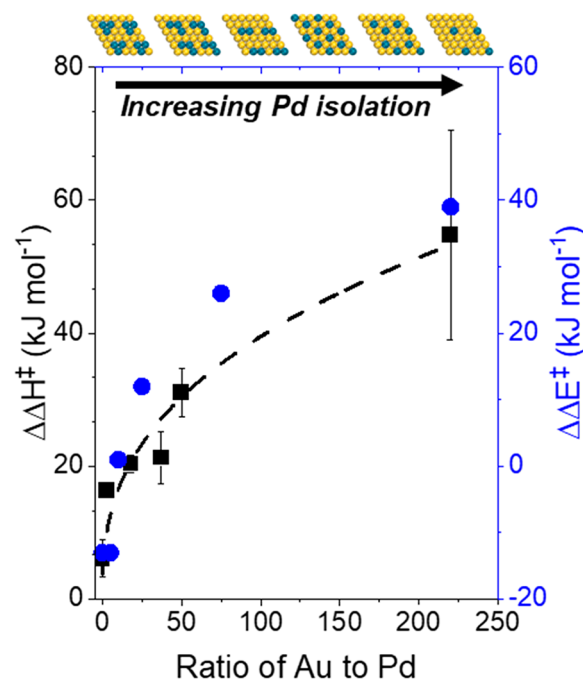


Figure 15. Differences between apparent activation enthalpies for H₂O₂ and H₂O formation (ΔΔH[‡] = ΔH[‡]_{H₂O} – ΔH[‡]_{H₂O₂}) measured experimentally (■) as a function of the Au to Pd ratio obtained on Pd₁Au_x catalysts (55 kPa H₂, 60 kPa O₂, 276–306 K) and calculated differences between the intrinsic activation energies for step 5 and step 4 (ΔΔE[‡] = ΔE[‡]₅ – ΔE[‡]₄, Scheme 1) obtained from DFT calculations (blue ●) carried out on representative PdAu_x(111) surfaces.

H₂O transition state. Thus, PdAu(111) surfaces that are more dilute in Pd show higher H₂O₂ selectivities; this trend continues past the point where all of the Pd exists as Pd monomers, showing that the second coordinative shell of Pd can have an effect on catalysis. This effect may arise from potentially different electronic structures of Pd in each PdAu(111) alloy or from geometric differences between surfaces.

To distinguish these two possible explanations, we show the projected DOS for each PdAu(111) surface in Figure 16 and

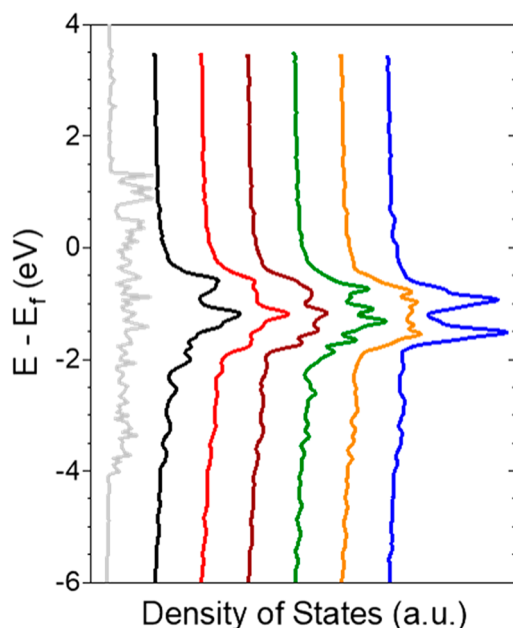


Figure 16. DFT-calculated projected density of states for Pd(111) (gray) and the closed triangular Pd trimer (black), open Pd trimer (red), dimer (brown), paired monomer (NNN = 6) (green), paired monomer (NNN = 3) (gold), and isolated monomer (blue) on Au surfaces.

compare to Pd. The *d*-band center for Pd atoms on PdAu(111) surfaces shows small and nonsystematic changes from closed and open Pd trimers (−1.511 and −1.514 eV, respectively) to dimers (−1.538 eV), paired monomers (−1.527, NNN = 6; −1.550 eV, NNN = 3), and isolated monomers (−1.580 eV). In contrast, the *d*-band center for Pd(111) is −1.714 eV.⁷⁵ The *d*-band structure for all PdAu(111) surfaces is narrow (fwhm ~1 eV), unlike Pd(111) (fwhm ~2.5 eV). These calculations suggest that the narrow, free-atom-like *d*-band structures calculated by Thirumalai and Kitchin for Pd, Pt, Ir, Rh, and Ni single atoms in Au, Cu, and Ag⁵³ and measured by Greiner et al. for Cu single atoms in Ag⁵⁴ are properties of dilute alloys and not only single-atom alloys: the narrow *d*-band structure emerges before reaching the single-atom limit. These electronic comparisons show that the dilution of Pd by Au causes changes in both the surface electronic and geometric structure, which affect rate and equilibrium constants for the elementary steps described in Scheme 1. The electronic and geometric contributions, therefore, cannot be fully decoupled for any catalyst. The differences between the positions of the *d*-band centers of the PdAu(111) surfaces shift minimally among the trimer and monomer structures (Figure 16); however, these surfaces clearly expose geometrically distinct ensembles of Pd atoms.

Consequently, the changes in geometric structure correlate more strongly with differences in H₂O₂ selectivity and activation barriers, which indicates that the coordination of the Pd atoms within these ensembles provides the selective stabilization of transition states for H₂O₂ over those that form H₂O. As Pd atoms become increasingly isolated by Au, activation barriers for both H₂O₂ and H₂O formation increase, but transition states that cleave O–O bonds sense these differences more strongly because they exchange greater amounts of charge (i.e., form more bonds) with the surface.

4.0. CONCLUSIONS

Comparisons among steady-state rates for the formation of H₂O₂ and H₂O, analysis of *in situ* X-ray absorption spectra, examination of *ex situ* infrared spectra of CO* species, and quantum chemical simulations carried out on representative surfaces demonstrate that the isolation of Pd atoms within Au domains forms active sites that preferentially form H₂O₂ and exhibit selectivities that increase with the separation between monomeric Pd atoms at surfaces. Electroless deposition of Pd onto Au nanoparticles results in uniform ensembles of nanoparticles that give high selectivities toward H₂O₂ (>60%) at Au to Pd ratios (Au:Pd > 18) that lead to materials with Pd–Pd coordination numbers nearing zero, as determined by *in situ* XAS and *ex situ* infrared spectra of chemisorbed CO. Further increases in Au to Pd ratios lead to greater selectivities that approach 100% for Pd₁Au₂₂₀. Statistical arguments and vibrational Stark effects indicate that these increases reflect the loss of next-nearest-neighbor Pd atoms (i.e., second coordination shell Pd). DFT calculations show H₂O₂ and H₂O form by solvent-mediated PET processes, which present lower barriers than plausible homolytic surface reaction on representative PdAu(111) surfaces in water. These findings agree with steady-state rates measured as functions of reactant pressures and the requirement for protic solvents for H₂O₂ formation. The mechanism and kinetically relevant steps for H₂O₂ and H₂O formation remain consistent across Pd and Pd₁Au_x catalysts.

Measured H₂O₂ selectivities primarily depend on differences between ΔH^\ddagger for parallel reaction pathways of a common surface intermediate (OOH*): reduction by PET to form H₂O₂ or a dissociative PET process that gives H₂O. Experimentally determined ΔH^\ddagger for both pathways increase with Au to Pd ratio but differ in their sensitivity to Pd isolation. These measured differences between ΔH^\ddagger for H₂O₂ and H₂O formation correlate strongly with DFT calculations of activation energies for the corresponding processes. These results indicate that both nearest and next-nearest Pd atoms stabilize transition states that dissociate OOH*; however, the formation of H₂O₂ seems to depend only upon the identity of nearest neighbor atoms. The different structural sensitivities of these steps predominantly reflect the number of surface atoms required to bind the transition and product state of these pathways.

Interpretation of these findings suggests that increased selectivities of H₂O₂ on AuPd catalysts described here (and in prior reports) largely originate from resulting geometric arrangements of Pd and Au atoms within active site ensembles and not from interatomic charge transfer, suppression of PdH_x formation, or changes in the reaction mechanism. Furthermore, measurements presented here demonstrate that careful synthesis of these dilute Pd atoms on surfaces of Au nanoparticles produces catalysts with an uncommon combi-

nation of high H₂O₂ selectivities and high stabilities in pure water. These materials represent a significant advance in the development of catalysts for the direct synthesis of H₂O₂ and suggest strategies for new catalyst compositions and structures.

■ ASSOCIATED CONTENT

Supporting Information

The Supporting Information is available free of charge at <https://pubs.acs.org/doi/10.1021/jacs.1c00539>.

Transmission electron micrographs, X-ray absorption spectra and fits, infrared spectra of adsorbed CO*, rate equation derivations, depictions of DFT reaction coordinates (PDF)

■ AUTHOR INFORMATION

Corresponding Author

David W. Flaherty – Department of Chemical and Biomolecular Engineering, University of Illinois Urbana–Champaign, Urbana, Illinois 61801, United States; orcid.org/0000-0002-0567-8481; Email: dwlflhrt@illinois.edu

Authors

Tomas Ricciardulli – Department of Chemical and Biomolecular Engineering, University of Illinois Urbana–Champaign, Urbana, Illinois 61801, United States

Sahithi Gorthy – Department of Chemical and Materials Science, University of Minnesota, Minneapolis, Minnesota 55455, United States

Jason S. Adams – Department of Chemical and Biomolecular Engineering, University of Illinois Urbana–Champaign, Urbana, Illinois 61801, United States; orcid.org/0000-0001-5320-200X

Coogan Thompson – Department of Chemical Engineering, Virginia Polytechnic Institute and State University, Blacksburg, Virginia 24060, United States

Ayman M. Karim – Department of Chemical Engineering, Virginia Polytechnic Institute and State University, Blacksburg, Virginia 24060, United States

Matthew Neurock – Department of Chemical and Materials Science, University of Minnesota, Minneapolis, Minnesota 55455, United States

Complete contact information is available at: <https://pubs.acs.org/doi/10.1021/jacs.1c00539>

Notes

The authors declare no competing financial interest.

■ ACKNOWLEDGMENTS

We gratefully acknowledge Dr. Waclaw Swietch, Dr. Adam Hoffman, and Prof. Simon Bare for training and assistance in data collection. This work was carried out in part in the Frederick Seitz Materials Research Laboratory Central Research Facilities, University of Illinois. We also acknowledge computational resources from the Minnesota Supercomputing Institute. T.R., J.S.A., and D.W.F. acknowledge generous support from the National Science Foundation (CBET-15531377), the Energy Biosciences Institute, and Shell International Exploration and Production, Inc. M.N. acknowledges support from National Science Foundation CSOE (CHE-2002158). A.M.K. acknowledges funding from the American Chemical Society Petroleum Research Fund award

number PRF# 55575-ND5. Use of the Stanford Synchrotron Radiation Light Source (Beamline 9-3, user proposal 4938) was supported by the U.S. Department of Energy, Office of Basic Energy Sciences, under Contract No. DE-AC02-76SF00515.

■ REFERENCES

- (1) Chorkendorff, I.; Niemantsverdriet, J. W. *Concepts of Modern Catalysis and Kinetics*; Wiley-VCH: Weinheim, Germany, 2003; pp 215–266.
- (2) Ponec, V. Alloy catalysts: the concepts. *Appl. Catal., A* **2001**, *222* (1–2), 31–45.
- (3) Hannagan, R. T.; Giannakakis, G.; Flytzani-Stephanopoulos, M.; Sykes, E. C. H. Single-Atom Alloy Catalysis. *Chem. Rev.* **2020**, *120* (21), 12044–12088.
- (4) Darby, M. T.; Stamatakis, M.; Michaelides, A.; Sykes, E. C. H. Lonely Atoms with Special Gifts: Breaking Linear Scaling Relationships in Heterogeneous Catalysis with Single-Atom Alloys. *J. Phys. Chem. Lett.* **2018**, *9* (18), 5636–5646.
- (5) Pei, G. X.; Liu, X. Y.; Wang, A.; Lee, A. F.; Isaacs, M. A.; Li, L.; Pan, X.; Yang, X.; Wang, X.; Tai, Z.; Wilson, K.; Zhang, T. Ag Alloyed Pd Single-Atom Catalysts for Efficient Selective Hydrogenation of Acetylene to Ethylene in Excess Ethylene. *ACS Catal.* **2015**, *5* (6), 3717–3725.
- (6) Studt, F.; Abild-Pedersen, F.; Bligaard, T.; Sørensen, R. Z.; Christensen, C. H.; Nørskov, J. K. On the Role of Surface Modifications of Palladium Catalysts in the Selective Hydrogenation of Acetylene. *Angew. Chem., Int. Ed.* **2008**, *47*, 9299–9302.
- (7) Palczewska, W.; Jablonski, A.; Kaszkur, Z.; Zuba, G.; Wernisch, J. Study on lead additives in modified palladium catalysts. *J. Mol. Catal.* **1984**, *25* (1–3), 307–316.
- (8) Galvita, V.; Siddiqi, G.; Sun, P.; Bell, A. T. Ethane dehydrogenation on Pt/Mg(Al)O and PtSn/Mg(Al)O catalysts. *J. Catal.* **2010**, *271* (2), 209–219.
- (9) Chen, M.; Kumar, D.; Yi, C.-W.; Goodman, D. W. The Promotional Effect of Gold in Catalysis by Palladium-Gold. *Science* **2005**, *310* (5746), 291–303.
- (10) D’Aniello, M. J.; Monroe, D. R.; Carr, C. J.; Krueger, M. H. The Redispersion of Sintered Pt, Rh, and Pt/Rh Catalysts. *J. Catal.* **1988**, *109*, 407–422.
- (11) Hendrickx, H. A. C. M.; Ponec, V. Effects of alloying and coadsorption: An IR study. *Surf. Sci.* **1987**, *192* (1), 234–242.
- (12) Toolenaar, F. J. C. M.; Stoop, F.; Ponec, V. On electronic and geometric effects of alloying: An infrared spectroscopic investigation of the adsorption of carbon monoxide on platinum-copper alloys. *J. Catal.* **1983**, *82* (1), 1.
- (13) Hammer, B.; Nørskov, J. K. Theoretical surface science and catalysis—calculations and concepts. *Adv. Catal.* **2000**, *45*, 71–129.
- (14) Calaza, F.; Mahapatra, M.; Neurock, M.; Tysøe, W. T. Disentangling ensemble, electronic and coverage effects on alloy catalysts: Vinyl acetate synthesis on Au/Pd(1 1 1). *J. Catal.* **2014**, *312*, 37–45.
- (15) Guesmi, H.; Louis, C.; Delannoy, L. Chemisorbed atomic oxygen inducing Pd segregation in PdAu(1 1 1) alloy: Energetic and electronic DFT analysis. *Chem. Phys. Lett.* **2011**, *503* (1–3), 97–100.
- (16) Dhoubi, A.; Guesmi, H. DFT study of the M segregation on MAu alloys (M = Ni, Pd, Pt) in presence of adsorbed oxygen O and O₂. *Chem. Phys. Lett.* **2012**, *521*, 98–103.
- (17) Yu, W.-Y.; Zhang, L.; Mullen, G. M.; Edward, J.; Evans, J.; Henkelman, G.; Mullins, C. B. Effect of annealing in oxygen on alloy structures of Pd-Au bimetallic model catalysts. *Phys. Chem. Chem. Phys.* **2015**, *17*, 20588–20596.
- (18) Boudart, M.; McDonald, M. A. Structure Sensitivity of Hydrocarbon Synthesis from CO and H₂. *J. Phys. Chem.* **1984**, *88*, 2185–2195.
- (19) Kugler, E. L.; Boudart, M. Ligand and ensemble effects in the adsorption of carbon monoxide on supported palladium-gold alloys. *J. Catal.* **1979**, *59* (2), 201–210.

- (20) Miura, H.; Endo, K.; Ogawa, R.; Shishido, T. Supported Palladium-Gold Alloy Catalysts for Efficient and Selective Hydro-silylation under Mild Conditions with Isolated Single Palladium Atoms in Alloy Nanoparticles as the Main Active Site. *ACS Catal.* **2017**, *7* (3), 1543–1553.
- (21) Yi, C.-W.; Luo, K.; Wei, T.; Goodman, D. W. The Composition and Structure of Pd-Au Surfaces. *J. Phys. Chem. B* **2005**, *109* (39), 18535–18540.
- (22) Gallo, I. B. C.; Carbonio, E. A.; Villullas, H. M. What Determines Electrochemical Surface Processes on Carbon-Supported PdAu Nanoparticles? *ACS Catal.* **2018**, *8*, 1818–1827.
- (23) Lee, A. F.; Baddeley, C. J.; Hardacre, C.; Ormerod, R. M.; Lambert, R. M.; Schmid, G.; West, H. Structural and Catalytic Properties of Novel Au/Pd Bimetallic Colloid Particles: EXAFS, XRD, and Acetylene Coupling. *J. Phys. Chem.* **1995**, *99*, 6096–6102.
- (24) Dash, P.; Bond, T.; Fowler, C.; Hou, W.; Coombs, N.; Scott, R. W. J. Rational Design of Supported PdAu Nanoparticle Catalysts from Structured Nanoparticle Precursors. *J. Phys. Chem. C* **2009**, *113* (29), 12719–12730.
- (25) Ball, M. R.; Wesley, T. S.; Rivera-Dones, K. R.; Huber, G. W.; Dumesic, J. A. Amination of 1-hexanol on bimetallic AuPd/TiO₂ catalysts. *Green Chem.* **2018**, *20*, 4695–4709.
- (26) Oxford, S. M.; Lee, P. L.; Chupas, P. J.; Chapman, K. W.; Kung, M. C.; Kung, H. H. Study of Supported PtCu and PdAu Bimetallic Nanoparticles Using In-Situ X-ray Tools. *J. Phys. Chem. C* **2010**, *114* (40), 17085–17091.
- (27) Fang, Y.-L.; Miller, J. T.; Guo, N.; Heck, K. N.; Alvarez, P. J. J.; Wong, M. S. Structural analysis of palladium-decorated gold nanoparticles as colloidal bimetallic catalysts. *Catal. Today* **2011**, *160* (1), 96–102.
- (28) Pei, G. X.; Liu, X. Y.; Wang, A.; Li, L.; Huang, Y.; Zhang, T.; Lee, J. W.; Jang, B. W. L.; Mou, C.-Y. Promotional effect of Pd single atoms on Au nanoparticles supported on silica for the selective hydrogenation of acetylene in excess ethylene. *New J. Chem.* **2014**, *38* (5), 2043–2051.
- (29) Pretzer, L. A.; Song, H. J.; Fang, Y.-L.; Zhao, Z.; Guo, N.; Wu, T.; Arslan, I.; Miller, J. T.; Wong, M. S. Hydrodechlorination catalysis of Pd-on-Au nanoparticles varies with particle size. *J. Catal.* **2013**, *298*, 206–217.
- (30) Gibson, E. K.; Beale, A. M.; Catlow, C. R. A.; Chutia, A.; Gianolio, D.; Gould, A.; Kroner, A.; Mohammed, K. M. H.; Perdjou, M.; Rogers, S. M.; Wells, P. P. Restructuring of AuPd Nanoparticles Studied by a Combined XAFS/DRIFTS Approach. *Chem. Mater.* **2015**, *27* (10), 3714–3720.
- (31) Zhao, Z.; Heck, K. N.; Limpornpipat, P.; Qian, H.; Miller, J. T.; Wong, M. S. Hydrogen-generating behavior of Pd-decorated gold nanoparticles via formic acid decomposition. *Catal. Today* **2019**, *330*, 24–31.
- (32) Zhu, M.-M.; Du, X.-L.; Zhao, Y.; Mei, B.-B.; Zhang, Q.; Sun, F.-F.; Jiang, Z.; Liu, Y.-M.; He, H.-Y.; Cao, Y. Ring-Opening Transformation of 5-Hydroxymethylfurfural Using a Golden Single-Atomic-Site Palladium Catalyst. *ACS Catal.* **2019**, *9* (7), 6212–6222.
- (33) Childers, D. J.; Schweitzer, N. M.; Shahri, S. M. K.; Rioux, R. M.; Miller, J. T.; Meyer, R. J. Evidence for geometric effects in neopentane conversion on PdAu catalysts. *Catal. Sci. Technol.* **2014**, *4*, 4366–4377.
- (34) Wrasman, C. J.; Boubnov, A.; Riscoe, A. R.; Hoffman, A. S.; Bare, S. R.; Cargnello, M. Synthesis of Colloidal Pd/Au Dilute Alloy Nanocrystals and Their Potential for Selective Catalytic Oxidations. *J. Am. Chem. Soc.* **2018**, *140* (40), 12930–12939.
- (35) Simson, S.; Jentys, A.; Lercher, J. A. Dynamic Phase Separation in Supported Pd-Au Catalysts. *J. Phys. Chem. C* **2015**, *119* (5), 2471–2482.
- (36) Knecht, M. R.; Weir, M. G.; Frenkel, A. I.; Crooks, R. M. Structural Rearrangement of Bimetallic Alloy PdAu Nanoparticles within Dendrimer Templates to Yield Core/Shell Configurations. *Chem. Mater.* **2008**, *20* (3), 1019–1028.
- (37) Luneau, M.; Shirman, T.; Filie, A.; Timoshenko, J.; Chen, W.; Trimpalis, A.; Flytzani-Stephanopoulos, M.; Kaxiras, E.; Frenkel, A. I.; Aizenberg, J.; Friend, C. M.; Madix, R. J. Dilute Pd/Au Alloy Nanoparticles Embedded in Colloid-Templated Porous SiO₂: Stable Au-Based Oxidation Catalysts. *Chem. Mater.* **2019**, *31* (15), 5759–5768.
- (38) Wei, X.; Yang, X.-F.; Wang, A.-Q.; Li, L.; Liu, X.-Y.; Zhang, T.; Mou, C.-Y.; Li, J. Bimetallic Au-Pd Alloy Catalysts for N₂O Decomposition: Effects of Surface Structures on Catalytic Activity. *J. Phys. Chem. C* **2012**, *116* (10), 6222–6232.
- (39) Ouyang, L.; Da, G.-j.; Tian, P.-f.; Chen, T.-y.; Liang, G.-d.; Xu, J.; Han, Y.-F. Insight into active sites of Pd-Au/TiO₂ catalysts in hydrogen peroxide synthesis directly from H₂ and O₂. *J. Catal.* **2014**, *311*, 129–136.
- (40) Kolli, N. E.; Delannoy, L.; Louis, C. Bimetallic Au-Pd catalysts for selective hydrogenation of butadiene: Influence of the preparation method on catalytic properties. *J. Catal.* **2013**, *297*, 79–92.
- (41) Wilson, N. M.; Priyadarshini, P.; Kunz, S.; Flaherty, D. W. Direct synthesis of H₂O₂ on Pd and Au_xPd_{1-x} clusters: Understanding the effects of alloying Pd with Au. *J. Catal.* **2018**, *357*, 163–175.
- (42) Kunz, S.; Iglesia, E. Mechanistic Evidence for Sequential Displacement-Reduction Routes in the Synthesis of Pd-Au Clusters with Uniform Size and Clean Surfaces. *J. Phys. Chem. C* **2014**, *118* (14), 7468–7479.
- (43) Liu, J.; Shan, J.; Lucci, F. R.; Cao, S.; Sykes, E. C. H.; Flytzani-Stephanopoulos, M. Palladium-gold single atom alloy catalysts for liquid phase selective hydrogenation of 1-hexyne. *Catal. Sci. Technol.* **2017**, *7*, 4276–4284.
- (44) Zhang, L.; Wang, A.; Miller, J. T.; Liu, X.; Yang, X.; Wang, W.; Li, L.; Huang, Y.; Mou, C.-Y.; Zhang, T. Efficient and Durable Au Alloyed Pd Single-Atom Catalyst for the Ullmann Reaction of Aryl Chlorides in Water. *ACS Catal.* **2014**, *4* (5), 1546–1553.
- (45) Han, Y.-F.; Zhong, Z.; Ramesh, K.; Chen, F.; Chen, L.; White, T.; Tay, Q.; Yaakub, S. N.; Wang, Z. Au Promotional Effects on the Synthesis of H₂O₂ Directly from H₂ and O₂ on Supported Pd-Au Alloy Catalysts. *J. Phys. Chem. C* **2007**, *111* (24), 8410–8413.
- (46) Alba-Rubio, A. C.; Plauck, A.; Stangland, E. E.; Mavrikakis, M.; Dumesic, J. A. Direct Synthesis of Hydrogen Peroxide Over Au-Pd Catalysts Prepared by Electroless Deposition. *Catal. Lett.* **2015**, *145* (12), 2057–2065.
- (47) Okamoto, H.; Massalski, T. B. The Au-Pd (Gold-Palladium) system. *J. Phase Equilib.* **1985**, *6* (3), 229–235.
- (48) Weissman-Wenocur, D. L.; Stefan, P. M.; Pate, B. B.; Shek, M. L.; Lindau, I.; Spicer, W. E. Photoemission study of Au overlayers on Pd(111) and the formation of a Pd-Au(111) alloy surface. *Phys. Rev. B: Condens. Matter Mater. Phys.* **1983**, *27* (6), 3308–3317.
- (49) Gao, F.; Goodman, D. W. Pd-Au bimetallic catalysts: understanding alloy effects from planar models and (supported) nanoparticles. *Chem. Soc. Rev.* **2012**, *41* (24), 8009–8020.
- (50) Ham, H. C.; Stephens, J. A.; Hwang, G. S.; Han, J.; Nam, S. W.; Lim, T. H. Pd ensemble effects on oxygen hydrogenation in AuPd alloys: A combined density functional theory and Monte Carlo study. *Catal. Today* **2011**, *165* (1), 138–144.
- (51) Boscoboinik, J. A.; Plaisance, C.; Neurock, M.; Tysoc, W. T. Monte Carlo and density functional theory analysis of the distribution of gold and palladium atoms on Au/Pd(111) alloys. *Phys. Rev. B: Condens. Matter Mater. Phys.* **2008**, *77*, 045422.
- (52) Marchal, R.; Genest, A.; Krüger, S.; Rösch, N. Structure of Pd/Au Alloy Nanoparticles from a Density Functional Theory-Based Embedded-Atom Potential. *J. Phys. Chem. C* **2013**, *117* (42), 21810–21822.
- (53) Thirumalai, H.; Kitchin, J. R. Investigating the Reactivity of Single Atom Alloys Using Density Functional Theory. *Top. Catal.* **2018**, *61* (5–6), 462–474.
- (54) Greiner, M. T.; Jones, T. E.; Beeg, S.; Zwiener, L.; Scherzer, M.; Girgsdies, F.; Piccinin, S.; Armbrüster, M.; Knop-Gericke, A.; Schlögl, R. Free-atom-like d states in single-atom alloy catalysts. *Nat. Chem.* **2018**, *10*, 1008–1015.
- (55) Pedersen, M. Ø.; Helveg, S.; Ruban, A.; Stensgaard, L.; Lægsgaard, E.; Nørskov, J. K.; Besenbacher, F. How a gold substrate

can increase the reactivity of a Pt overlayer. *Surf. Sci.* **1999**, *426* (3), 395–409.

(56) Edwards, J. K.; Solsona, B.; N, E. N.; Carley, A. F.; Herzing, A. A.; Kiely, C. J.; Hutchings, G. J. Switching Off Hydrogen Peroxide Hydrogenation in the Direct Synthesis Process. *Science* **2009**, *323* (5917), 1037–1041.

(57) Solsona, B. E.; Edwards, J. K.; Landon, P.; Carley, A. F.; Herzing, A.; Kiely, C. J.; Hutchings, G. J. Direct Synthesis of Hydrogen Peroxide from H₂ and O₂ Using Al₂O₃ Supported Au-Pd Catalysts. *Chem. Mater.* **2006**, *18* (11), 2689–2695.

(58) Plauck, A.; Stangland, E. E.; Dumesic, J. A.; Mavrikakis, M. Active sites and mechanisms for H₂O₂ decomposition over Pd catalysts. *Proc. Natl. Acad. Sci. U. S. A.* **2016**, *113* (14), 1973–1982.

(59) Priyadarshini, P.; Flaherty, D. W. Form of the catalytically active Pd species during the direct synthesis of hydrogen peroxide. *AIChE J.* **2019**, *65*, 16829.

(60) Wang, S.; Doronkin, D. E.; Hähler, M.; Huang, X.; Wang, D.; Grunwaldt, J. D.; Behrens, S. Palladium-Based Bimetallic Nanocrystal Catalysts for the Direct Synthesis of Hydrogen Peroxide. *ChemSusChem* **2020**, *13* (12), 3243–3251.

(61) Priyadarshini, P.; Ricciardulli, T.; Adams, J.; Yun, Y.; Flaherty, D. W. Effects of Bromide Adsorption on the Direct Synthesis of H₂O₂ on Pd Nanoparticles: Formation Rates, Selectivities, and Apparent Barriers at Steady-State. **2021**, in review.

(62) Centomo, P.; Meneghini, C.; Sterchele, S.; Trapananti, A.; Aquilanti, G.; Zecca, M. In Situ X-ray Absorption Fine Structure Spectroscopy of a Palladium Catalyst for the Direct Synthesis of Hydrogen Peroxide: Leaching and Reduction of the Metal Phase in the Presence of Bromide Ions. *ChemCatChem* **2015**, *7* (22), 3712–3718.

(63) Bernardotto, G.; Menegazzo, F.; Pinna, F.; Signoretto, M.; Cruciani, G.; Strukul, G. New Pd-Pt and Pd-Au catalysts for an efficient synthesis of H₂O₂ from H₂ and O₂ under very mild conditions. *Appl. Catal., A* **2009**, *358* (2), 129–135.

(64) Kanungo, S.; Haandel, L.; Hensen, E. J. M.; Schouten, J. C.; D'Angelo, M. F. N. Direct synthesis of H₂O₂ in AuPd coated micro channels: An in-situ X-Ray absorption spectroscopic study. *J. Catal.* **2019**, *370*, 200–209.

(65) Wilson, N. M.; Pan, Y.-T.; Shao, Y.-T.; Zuo, J.-M.; Yang, H.; Flaherty, D. W. Direct Synthesis of H₂O₂ on AgPt Octahedra: The Importance of Ag-Pt Coordination for High H₂O₂ Selectivity. *ACS Catal.* **2018**, *8* (4), 2280–2289.

(66) Wilson, N. M.; Schröder, J.; Priyadarshini, P.; Bregante, D. T.; Kunz, S.; Flaherty, D. W. Direct synthesis of H₂O₂ on PdZn nanoparticles: The impact of electronic modifications and heterogeneity of active sites. *J. Catal.* **2018**, *368*, 261–274.

(67) Wang, S.; Lewis, R. J.; Doronkin, D. E.; Morgan, D. J.; Grunwaldt, J.-D.; Hutchings, G. J.; Behrens, S. The direct synthesis of hydrogen peroxide from H₂ and O₂ using Pd-Ga and Pd-In catalysts. *Catal. Sci. Technol.* **2020**, *10* (6), 1925–1932.

(68) Tian, P.; Xu, X.; Ao, C.; Ding, D.; Li, W.; Si, R.; Tu, W.; Xu, J.; Han, Y.-F. Direct and Selective Synthesis of Hydrogen Peroxide over Palladium-Tellurium Catalysts at Ambient Pressure. *ChemSusChem* **2017**, *10*, 3342–3346.

(69) Ding, D.; Xu, X.; Tian, P.; Liu, X.; Xua, J.; Han, Y.-F. Promotional effects of Sb on Pd-based catalysts for the direct synthesis of hydrogen peroxide at ambient pressure. *Chin. J. Catal.* **2018**, *39* (4), 673–681.

(70) Menegazzo, F.; Signoretto, M.; Manzoli, M.; Bocuzzi, F.; Cruciani, G.; Pinna, F.; Strukul, G. Influence of the preparation method on the morphological and composition properties of Pd-Au/ZrO₂ catalysts and their effect on the direct synthesis of hydrogen peroxide from hydrogen and oxygen. *J. Catal.* **2009**, *268* (1), 122–130.

(71) Sterchele, S.; Biasi, P.; Centomo, P.; Canton, P.; Campestrini, S.; Salmi, T.; Zecca, M. Pd-Au and Pd-Pt catalysts for the direct synthesis of hydrogen peroxide in absence of selectivity enhancers. *Appl. Catal., A* **2013**, *468*, 160–174.

(72) Paunovic, V.; Ordonsky, V.; D'Angelo, M. F. N.; Schouten, J. C.; Nijhuis, T. A. Direct synthesis of hydrogen peroxide over Au-Pd catalyst in a wall-coated microchannel. *J. Catal.* **2014**, *309*, 325–332.

(73) Edwards, J. K.; Freakley, S. J.; Carley, A. F.; Kiely, C. J.; Hutchings, G. J. Strategies for Designing Supported Gold Palladium Bimetallic Catalysts for the Direct Synthesis of Hydrogen Peroxide. *Acc. Chem. Res.* **2014**, *47* (3), 845–854.

(74) Selinsek, M.; Deschner, B. J.; Doronkin, D. E.; Sheppard, T. L.; Grunwaldt, J.-D.; Dittmeyer, R. Revealing the Structure and Mechanism of Palladium during Direct Synthesis of Hydrogen Peroxide in Continuous Flow Using Operando Spectroscopy. *ACS Catal.* **2018**, *8* (3), 2546–2557.

(75) Adams, J. S.; Chemburkar, A.; Priyadarshini, P.; Ricciardulli, T.; Lu, Y.; Maliekkal, V.; Sampath, A.; Winikoff, S.; Karim, A. M.; Neurock, M.; Flaherty, D. W. Solvent molecules form surface redox mediators in situ and cocatalyze O₂ reduction on Pd. *Science* **2021**, *371* (6529), 626–632.

(76) Campos-Martin, J. M.; Blanco-Brieva, G.; Fierro, J. L. G. Hydrogen Peroxide Synthesis: An Outlook beyond the Anthraquinone Process. *Angew. Chem., Int. Ed.* **2006**, *45* (42), 6962–6984.

(77) Wilson, N. M.; Flaherty, D. W. Mechanism for the Direct Synthesis of H₂O₂ on Pd Clusters: Heterolytic Reaction Pathways at the Liquid-Solid Interface. *J. Am. Chem. Soc.* **2016**, *138* (2), 574–586.

(78) Ford, D. C.; Nilekar, A. U.; Xu, Y.; Mavrikakis, M. Partial and complete reduction of O₂ by hydrogen on transition metal surfaces. *Surf. Sci.* **2010**, *604* (19–20), 1565–1575.

(79) Nørskov, J. K.; Rossmeisl, J.; Logadottir, A.; Lindqvist, L.; Kitchin, J. R.; Bligaard, T.; Jónsson, H. Origin of the Overpotential for Oxygen Reduction at a Fuel-Cell Cathode. *J. Phys. Chem. B* **2004**, *108* (46), 17886–17892.

(80) Reifsnnyder, S. N.; Lamb, H. H. Characterization of Silica-Supported Pd-Au Clusters by X-ray Absorption Spectroscopy. *J. Phys. Chem. B* **1999**, *103* (2), 321–329.

(81) Zanella, R.; Delannoy, L.; Louis, C. Mechanism of deposition of gold precursors onto TiO₂ during the preparation by cation adsorption and deposition-precipitation with NaOH and urea. *Appl. Catal., A* **2005**, *291* (1–2), 62–72.

(82) Block, B. P.; Bailar, J. C. The Reaction of Gold(III) with Some Bidentate Coordinating Groups. *J. Am. Chem. Soc.* **1951**, *73* (10), 4722–4725.

(83) Lam, Y. L.; Boudart, M. Preparation of small Au-Pd particles on silica. *J. Catal.* **1977**, *50* (3), 530–540.

(84) Nutt, M. O.; Heck, K. N.; Alvarez, P.; Wong, M. S. Improved Pd-on-Au bimetallic nanoparticle catalysts for aqueous-phase trichloroethene hydrodechlorination. *Appl. Catal., B* **2006**, *36* (1–2), 115–125.

(85) Rebelli, J.; Detwiler, M.; Ma, S.; Williams, C. T.; Monnier, J. R. Synthesis and characterization of Au-Pd/SiO₂ bimetallic catalysts prepared by electroless deposition. *J. Catal.* **2010**, *270* (2), 224–233.

(86) Thanh, N. T. K.; Maclean, N.; Mahiddine, S. Mechanisms of Nucleation and Growth of Nanoparticles in Solution. *Chem. Rev.* **2014**, *114* (15), 7610–7630.

(87) Bregante, D. T.; Tan, J. Z.; Sutrisno, A.; Flaherty, D. W. Heteroatom substituted zeolite FAU with ultralow Al contents for liquid-phase oxidation catalysis. *Catal. Sci. Technol.* **2020**, *10* (3), 635–647.

(88) Bregante, D. T.; Johnson, A. M.; Patel, A. Y.; Ayla, E. Z.; Cordon, M. J.; Bukowski, B. C.; Greeley, J.; Gounder, R.; Flaherty, D. W. Cooperative Effects between Hydrophilic Pores and Solvents: Catalytic Consequences of Hydrogen Bonding on Alkene Epoxidation in Zeolites. *J. Am. Chem. Soc.* **2019**, *141*, 7302–7319.

(89) Witzke, M. E.; Almithn, A.; Conrad, C. L.; Triesenberg, M. D.; Hibbitts, D. D.; Flaherty, D. W. In Situ Methods for Identifying Reactive Surface Intermediates during Hydrogenolysis Reactions: C–O Bond Cleavage on Nanoparticles of Nickel and Nickel Phosphides. *J. Am. Chem. Soc.* **2019**, *141*, 16671–16684.

(90) Whittaker, T.; Kumar, K. B. S.; Peterson, C.; Pollock, M. N.; Grabow, L. C.; Chandler, B. D. H₂ Oxidation over Supported Au Nanoparticle Catalysts: Evidence for Heterolytic H₂ Activation at the

Metal-Support Interface. *J. Am. Chem. Soc.* **2018**, *140* (48), 16469–16487.

(91) Karim, A. M.; Howard, C.; Roberts, B.; Kovarik, L.; Zhang, L.; King, D. L.; Wang, Y. In Situ X-ray Absorption Fine Structure Studies on the Effect of pH on Pt Electronic Density during Aqueous Phase Reforming of Glycerol. *ACS Catal.* **2012**, *2* (11), 2387–2394.

(92) Zabinsky, S. I.; Rehr, J. J.; Ankudinov, A.; Albers, R. C.; Eller, M. J. Multiple-scattering calculations of x-ray-absorption spectra. *Phys. Rev. B: Condens. Matter Mater. Phys.* **1995**, *52* (4), 2995–3009.

(93) Li, W.; Ivanov, S.; Mozaffari, S.; Shanaiah, N.; Karim, A. M. Palladium Acetate Trimer: Understanding Its Ligand-Induced Dissociation Thermochemistry Using Isothermal Titration Calorimetry, X-ray Absorption Fine Structure, and ³¹P Nuclear Magnetic Resonance. *Organometallics* **2019**, *38* (2), 451–460.

(94) Kresse, G.; Hafner, J. Ab Initio Molecular Dynamics for Liquid Metals. *Phys. Rev. B: Condens. Matter Mater. Phys.* **1993**, *47*.

(95) Kresse, G.; Hafner, J. Ab Initio Molecular-Dynamics Simulation of the Liquid-Metal-amorphous-Semiconductor Transition in Germanium. *Phys. Rev. B: Condens. Matter Mater. Phys.* **1994**, *49*, 14251–14269.

(96) Kresse, G.; Furthmüller, J. Efficient Iterative Schemes for Ab Initio Total-Energy Calculations Using a Plane-Wave Basis Set. *Phys. Rev. B: Condens. Matter Mater. Phys.* **1996**, *54*, 11169–11186.

(97) Kresse, G.; Joubert, D. From Ultrasoft Pseudopotentials to the Projector Augmented-Wave Method. *Phys. Rev. B: Condens. Matter Mater. Phys.* **1999**, *59*, 1758–1775.

(98) Blöchl, P. E. Projector Augmented-Wave Method. *Phys. Rev. B: Condens. Matter Mater. Phys.* **1994**, *50*, 17953–17979.

(99) Perdew, J. P.; Burke, K.; Ernzerhof, M. Generalized Gradient Approximation Made Simple. *Phys. Rev. Lett.* **1996**, *77*, 3865–3868.

(100) Grimme, S. Semiempirical GGA-Type Density Functional Constructed with a Long-Range Dispersion Correction. *J. Comput. Chem.* **2006**, *27*, 1787–1799.

(101) Grimme, S. Density Functional Theory with London Dispersion Corrections. *Wiley Interdiscip. Rev.: Comput. Mol. Sci.* **2011**, *1*, 211–228.

(102) Henkelman, G.; Jonsson, H. A Dimer Method for Finding Saddle Points on High Dimensional Potential Surfaces Using Only First Derivatives. *J. Chem. Phys.* **1999**, *111*, 7010–7022.

(103) Henkelman, G.; Jonsson, H. Improved Tangent Estimate in the Nudged Elastic Band Method for Finding Minimum Energy Paths and Saddle Points Improved Tangent Estimate in the Nudged Elastic Band Method for Finding Minimum Energy Paths and Saddle Points. *J. Chem. Phys.* **2000**, *113*, 9978–9985.

(104) Henkelman, G.; Uberuaga, B. P.; Jonsson, H. A Climbing Image Nudged Elastic Band Method for Finding Saddle Points and Minimum Energy Paths A Climbing Image Nudged Elastic Band Method for Finding Saddle Points and Minimum Energy Paths. *J. Chem. Phys.* **2000**, *113*, 9901–9904.

(105) Ouyang, L.; Tian, P.-f.; Da, G.-j.; Xu, X.-C.; Ao, C.; Chen, T.-y.; Si, R.; Xu, J.; Han, Y.-F. The origin of active sites for direct synthesis of H₂O₂ on Pd/TiO₂ catalysts: Interfaces of Pd and PdO domains. *J. Catal.* **2015**, *321*, 70–80.

(106) Song, X.; Sun, K.; Hao, X.; Su, H.-Y.; Ma, X.; Xu, Y., Facet-Dependent of Catalytic Selectivity: The Case of H₂O₂ Direct Synthesis on Pd Surfaces. *J. Phys. Chem. C* **2019**, *123* (43), 26324–26337.

(107) Edwards, J. K.; Pritchard, J.; Lu, L.; Piccinini, M.; Shaw, G.; Carley, A. F.; Morgan, D. J.; Kiely, C. J.; Hutchings, G. J. The Direct Synthesis of Hydrogen Peroxide Using Platinum-Promoted Gold-Palladium Catalysts. *Angew. Chem., Int. Ed.* **2014**, *53*, 2381–2384.

(108) Meier, D. C.; Goodman, D. W. The Influence of Metal Cluster Size on Adsorption Energies: CO Adsorbed on Au Clusters Supported on TiO₂. *J. Am. Chem. Soc.* **2004**, *129* (6), 1892–1899.

(109) Gao, F.; Wang, Y.; Goodman, D. W. Reaction Kinetics and Polarization-Modulation Infrared Reflection Absorption Spectroscopy (PM-IRAS) Investigation of CO Oxidation over Supported Pd-Au Alloy Catalysts. *J. Phys. Chem. C* **2010**, *114* (9), 4036–4043.

(110) Yudanov, I. V.; Sahnoun, R.; Neyman, K. M.; Rösch, N.; Hoffmann, J.; Schauermaier, S.; Johánek, V.; Unterhalt, H.; Rupprechter, G.; Libuda, J.; Freund, H.-J. CO Adsorption on Pd Nanoparticles: Density Functional and Vibrational Spectroscopy Studies. *J. Phys. Chem. B* **2003**, *107* (1), 255–264.

(111) Yuan, D.; Gong, X.; Wu, R. Atomic configurations of Pd atoms in PdAu(111) bimetallic surfaces investigated using the first-principles pseudopotential plane wave approach. *Phys. Rev. B: Condens. Matter Mater. Phys.* **2007**, *75*, 085428.

(112) García-Mota, M.; López, N. Temperature and pressure effects in CO titration of ensembles in PdAu(111) alloys using first principles. *Phys. Rev. B: Condens. Matter Mater. Phys.* **2010**, *82*, 075411.

(113) Hoffmann, F. M. Infrared reflection-absorption spectroscopy of adsorbed molecules. *Surf. Sci. Rep.* **1983**, *3* (2–3), 107–192.

(114) Olsen, C. W.; Masel, R. I. An infrared study of CO adsorption on Pt(111). *Surf. Sci.* **1988**, *201* (3), 444–460.

(115) Manzi, S.; Helú, M. A. B.; Tysøe, W. T.; Calaza, F. C. Combining IR Spectroscopy and Monte Carlo Simulations to Identify CO Adsorption Sites on Bimetallic Alloys. *J. Phys. Chem. C* **2019**, *123*, 8406–8420.

(116) Zhu, X.; Guo, Q.; Sun, Y.; Chen, S.; Wang, J.-Q.; Wu, M.; Fu, W.; Tang, Y.; Duan, X.; Chen, D.; Wan, Y. Optimising surface d charge of AuPd nanoalloy catalysts for enhanced catalytic activity. *Nat. Commun.* **2019**, *10*, 1428.

(117) Kim, C. S.; Tornquist, W. J.; Korzeniewski, C. Site-dependent vibrational coupling of CO adsorbates on well-defined step and terrace sites of monocrystalline platinum: Mixed-isotope studies at Pt(335) and Pt(111) in the aqueous electrochemical environment. *J. Chem. Phys.* **1994**, *101*, 9113.

(118) Dissanayake, D. P.; Lunsford, J. H. The direct formation of H₂O₂ from H₂ and O₂ over colloidal palladium. *J. Catal.* **2003**, *214*, 113–120.

(119) Dumesic, J. A.; Rudd, D. F.; Aparicio, L. M.; Rekoske, J. E. *The Microkinetics of Heterogeneous Catalysis*; American Chemical Society: Washington, DC, 1993; pp 113–144.

(120) Hansen, E. W.; Neurock, M. First-Principles-Based Monte Carlo Simulation of Ethylene Hydrogenation Kinetics on Pd. *J. Catal.* **2000**, *196*, 241–252.

(121) Derry, G. N.; Kern, M. E.; Worth, E. H. Recommended values of clean metal surface work functions. *J. Vac. Sci. Technol., A* **2015**, *33*, 060801–060810.